Heliyon 10 (2024) e33820

Contents lists available at ScienceDirect

Heliyon

journal homepage: www.cell.com/heliyon

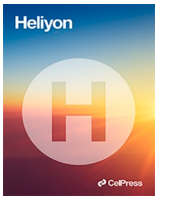

Research article

Artificial neural network modelling and experimental investigations of malachite green adsorption on novel carboxymethyl cellulose/β-cyclodextrin/nickel cobaltite composite

Ruksana Sirach, Pragnesh N. Dave *

Department of Chemistry, Sardar Patel University, Vallabh Vidyanagar, 388 120, Gujarat, India

ARTICLE INFO

Keywords:
Carboxymethyl cellulose
Nickel cobaltite ($NiC_{O2}O_4$)
Adsorption
Artificial neural network
Malachite green

ABSTRACT

This study presents a novel polymer nanocomposite based on carboxymethyl cellulose and β-cyclodextrin crosslinked with succinic acid (CMC-SA-β-CD) containing nickel cobaltite (NCO) nano-reinforcement. Various analytical techniques have been employed to investigate the structural, thermal, and morphological features of the resulting nanocomposite. The CMC-SA-β-CD/NCO nanocomposite has been utilized as an adsorbent for the removal of bisphenol-A (BPA, $R\% < 40$ %), malachite green (MG, $R\% > 75$ %)), and Congo red (CR, no adsorption) from the synthetic wastewater. The study systematically explored the impact of various parameters on the adsorption process, and the interactions between MG and CMC-SA-β-CD/NCO were discussed. The adsorption data were fitted to different models to elucidate the kinetics and thermodynamics of the adsorption process. An artificial neural network (ANN) analysis was employed to train the experimental dataset for predicting adsorption outcomes. Despite a low BET surface area (0.798 $m^2\ g^{-1}$), CMC-SA-β-CD/NCO was found to exhibit high MG adsorption capacity. CMC-SA-β-CD/NCO exhibited better MG adsorption performance at pH 5.5, 40 mg L^{-1} MG dye concentration, 170 min equilibrium time, 20 mg CMC-SA-β-CD/NCO dose with more than 90 % removal efficiency. Moreover, the thermodynamic studies suggest that the adsorption of MG was exothermic with ΔH° value -9.93 ± 0.76 kJ mol^{-1}. The isotherm studies revealed that the Langmuir model was the best model to describe the adsorption of MG on CMC-SA-β-CD/NCO indicating monolayer surface coverage with Langmuir adsorption capacity of 182 ± 4 mg g^{-1}. The energy of adsorption (11.4 ± 0.8 kJ mol^{-1}) indicated chemisorption of MG on the composite surface. The kinetics studies revealed that the pseudo-first-order model best described the adsorption kinetics with $q_e = 86.7 \pm 2.9$ mg g^{-1}. A good removal efficiency (>70 %) was retained after five regeneration reuse cycles. The ANN-trained data showed good linearity between predicted and actual data for the adsorption capacity (R-value>0.99), indicating the reliability of the prediction model. The developed nanocomposite, composed predominantly of biodegradable material, is facile to synthesize and exhibited excellent monolayer adsorption of MG providing a new sustainable adsorbent for selective MG removal.

* Corresponding author.
E-mail address: pragnesh7@yahoo.com (P.N. Dave).

https://doi.org/10.1016/j.heliyon.2024.e33820
Received 17 March 2024; Received in revised form 26 June 2024; Accepted 27 June 2024
Available online 28 June 2024

1. Introduction

The availability of potable water is a pressing concern for numerous countries due to increasing population, urbanization, industrialization, and utilization of more fresh water resources [1–4]. Freshwater resources are being utilized, and wastewater is often discarded without adequate treatment, exacerbating the issue of water scarcity. According to one article, in Bangladesh during wet processing, a large amount of water is utilized and wastewater is created as not 100 % dye is fixated on the fabric [4]. i.e., for eighteen Industries, the amount of dye used was about 2,29,2000 kg. Up to forty percent of the reactive dyes may be lost due to incomplete fixing. Approximately 4,60,000 kg of dyes will be lost annually if a twenty percent loss is taken into account, hence, creating color contamination in the water [4]. The color contamination often interferes with the photosynthesis process of marine plant kingdom [3]. The dyes can be mainly classified into non-ionic, anionic, and cationic depending on the charge [1,3]. In addition to being carcinogenic, cationic dyes can cause vomiting, eye irritation, and heart and breathing related issues [1]. One of the most extensively studied dyes among cationic dyes is methylene blue. There are relatively fewer reports available on the adsorption of the cationic malachite green (MG) dye. Various research studies published previously by various authors confirm that MG can inhibit good microorganisms and can potentially disturb marine life [5–9]. Therefore, removing MG from the water is necessary. If treated to meet proper standards, wastewater could be repurposed for various industrial and agricultural needs.

Various methods like photocatalytic degradation, advanced oxidation processes, membrane-filtration, flocculation-coagulation, adsorption, and biological treatment are available for the treatment of the color contaminated wastewater [1]. Adsorption is one of the easy, effective, and cost-effective methods to remove contaminants from the aqueous medium [10,11]. The use of adsorbent materials to eliminate impurities from water has been a well-established practice for generations. However, researchers continue to seek improved options in terms of sustainability and performance. There is a growing unease regarding the utilization of less sustainable materials. Among the various adsorbents employed for purification purposes, polysaccharide-based materials are widely recognized for their biodegradability and biocompatibility [12]. Carboxymethyl cellulose (CMC) is a water-soluble derivative of the cellulose macromolecule, composed of a linear polysaccharide chain containing β-1,4-glycosidic linkages [13]. However, the direct application of CMC is not feasible in certain contexts, such as in adsorbent applications, due to its solubility in water. Moreover, selectivity is also a concern when utilizing the adsorption method. Some hydrogels lack selectivity and show high adsorption performance irrespective of the charge of the adsorbate molecule (supplementary file; section S1). To address these limitations, various composite materials, including nanocomposites, are currently under investigation. Previously, CMC-based composites containing carbon-based materials [14–18], clays [19–23], and metal oxides [24–26] have been reported.

β-cyclodextrin (β-CD) is a biodegradable and eco-friendly macromolecule that provides unique host-guest interactions because of the structure of β-CD [27–29], but its use in water contamination removal is not widely explored. Both β-CD and CMC possess a large number of hydroxyl groups. In addition to hydroxyl groups, CMC contains $-COO^{1-}$ functional groups, which allow the linking of CMC and β-CD using acids like citric acid and epichlorohydrin (ECH) (section S2) [30,31]. Recently, AB_2O_4 type metal oxides (where B═Fe, Co, Cr, etc.) have been studied by researchers because of their optical, structural, and magnetic features [32]. Hence, consequently, the investigation focused on a nanocomposite based on ACo_2O_4 type material (i.e., $NiCo_2O_4$) incorporated into a CMC/β-CD based polymeric matrix.

In this study, for the first time, the preparation of CMC/*β-CD* crosslinked using succinic acid (SA) (CMC-SA-β-CD) and its composite with $NiCo_2O_4$ (CMC-SA-β-CD/NCO) is reported. Various techniques were employed to characterize the composite and explore its surface and structural properties. The CMC-SA-β-CD/NCO nanocomposite was utilized as an adsorbent to remove a cationic dye (MG). Artificial neural networks (ANN) were used to train the obtained adsorption and removal data for the adsorption of MG on CMC-SA-β-CD/NCO.

2. Materials and Methodology

2.1. Materials

All the materials used in the given work were acquired from their respective providers and used as such without further modifications.

β-CD (Merck, India; ≥97 %), CMC (Himedia, India) and SA (SRL, India; 99.5 %), Malachite green oxalate (Himedia, India), Congo red (CR, Merck, India), NaOH (Samir TECH-CHEM, India; 99 %), Nickel nitrate hexahydrate [$Ni(NO_3)_2.6H_2O$; LobaChemie, India, 98 %], cobalt nitrate hexahydrate [$Co(NO_3)_2.6H_2O$; LobaChemie, India], sodium chloride (NaCl, Samir TECH-CHEM, India, >99 %), potassium chloride (KCl, Astron, India, >99 %), calcium chloride ($CaCl_2$, Astron, India, 90 %) and magnesium chloride hexahydrate ($MgCl_2.6H_2O$, >97 %, Samir TECH-CHEM) were used for the given work. Throughout the experiments distilled water was used.

2.2. Synthesis of $NiCo_2O_4$

2.2.1. Preparation of bottle guard peel extract

The synthesis of $NiCo_2O_4$ was carried out in the presence of bottle guard peel extract (Fig. S1). To the best of the author's knowledge, this is the first report of the synthesis of $NiCo_2O_4$ in the presence of bottle guard peel extract. Bottle guard peels were thoroughly washed using distilled water to remove dirt and other contaminants. 132 g waste bottle guard peels were sundried for a week and then ground into fine powder using a mortar pestle (12 g). 75 mL of ethanol and 225 mL of water (molar ratio of ethanol: water = 1:9.7) were combined in a 250 mL conical flask. The dried bottle gourd peel powder was introduced into the conical flask and

stirred using a magnetic stirrer at room temperature (32 °C) for 17 h, followed by heating at $T = 50$ °C for 60 min. The resulting mixture was then subjected to filtration, and the filtrate was stored in a refrigerator for subsequent use.

2.2.2. Co-precipitation method

17.45 g of $Co(NO_3)_2{\cdot}6H_2O$ and 8.72 g of $Ni(NO_3)_2{\cdot}6H_2O$ (mole ratio of Co^{2+}:Ni^{2+} was 2:1)were dissolved in 125 mL of bottle guard peel water extract (section 2.2.1) in a 500 mL conical flask. The contents were stirred at 50 °C for 60 min. A 2 M NaOH solution was gradually added to this mixture using a burette at an addition rate of 1 mL/40 s. The addition of NaOH was continued until the pH of the solution reached approximately pH 11. The resulting greenish precipitates were irradiated with ultrasound for 10 min, filtered, and washed several times with water. The washed precipitate was then added to 500 mL of water in a conical flask, irradiated again with ultrasound for 20 min, covered with aluminum foil, and placed inside an oven heated at 60 °C for 15 h. The resulting content was filtered, dried in an oven at 80 °C for 15 h, and subjected to calcination at 450 °C for 5 h. The obtained blackish substance, $NiCo_2O_4$ (NCO), was characterized and used for composite synthesis.

2.3. Synthesis of CMC-SA-β-CD

β-CD and CMC were pre-dried in an oven before the synthesis of CMC-SA-β-CD to eliminate moisture. In a process, 0.88 g of β-CD was dissolved in 200 mL of water at 60 °C using mechanical stirring. To this, 4.4 g of CMC was added until a clear slurry was obtained. Subsequently, 1.76 g of SA was added, and the resulting mixture was subjected to ultrasound irradiation for 20 min. The content was allowed to react overnight and then transferred into a Petri dish, heated in an oven at 60 °C for 16 h (refer to the supplementary file). The obtained polymer matrix was soaked in distilled water and washed several times with warm water to remove impurities. The resulting CMC-SA-β-CD was ground using a mortar and pestle. For comparison, CMC-SA was prepared without adding β-CD in the initial step.

2.4. Synthesis of CMC-SA-β-CD/NCO

The synthesis of CMC-SA-β-CD/NCO followed a procedure similar to that reported in section 2.3. Specifically, 0.05 g of *β-CD* was dissolved in water (T = 60 °C; mechanical stirring). $NiCo_2O_4$ (5, 10, 15, or 20 mg), synthesized as per section 2.2, was added to the solution, and the final mixture was subjected to ultrasound irradiation to ensure well-dispersion of $NiCo_2O_4$. Subsequently, CMC (0.25 g) and SA (0.1 g) were added, and the sample was treated in a manner consistent with the procedure detailed in section 2.3. The dose of $NiCo_2O_4$ varied between 5 and 20 mg and was tested for adsorption (discussion given in section 3.5.1).

2.5. Characterizations

The formation of the nanocomposite was confirmed through powder X-ray diffraction (XRD; PANalyticalX'Pert Pro; 40 mA; 40 kV;λ = 0.154 nm for Cu Kα source; $10° \leq 2\theta \leq 90°$; scan step time = 0.6s; step size 2θ = 0.03°) and Fourier-transform infrared spectroscopy (FTIR; FT-IR Spectrum 2 (PerkinElmer); 4000-400 cm^{-1}). Field emission scanning electron microscopy (FE-SEM) combined with Energy-dispersive X-ray spectroscopy (EDS) was employed to capture the surface morphology and identify the presence of elements (Nova Nano FE-SEM 450 (FEI)). Dynamic light scattering (DLS; HORIBA DLS Particle size analyzer; SZ-100Z) was utilized to measure the zeta potential and particle size distribution of the samples. Micromeritics, ASAP 2010 was employed to evaluate the specific surface area (N_2 adsorption; sample mass ~0.4–0.5 g; Brunauer-Emmett-Teller (BET)). A simultaneous thermal analyzer (5000/2960 STA; TA instrument; under an inert atmosphere) was used to study the thermal stability. Adsorption studies were conducted under various conditions and the concentration of adsorbate MG was studied using a UV–Vis spectrophotometer ($\lambda = 200-800$ nm; SHIMADZU TCC-240 A; $\lambda_{max} = 617$ nm for MG).

2.6. Adsorption studies

The adsorption experiments were conducted in 100 mL conical flasks with 40 mL of MG dye solutions. Each experiment used a fixed volume of 40 mL of fresh MG solution, which was prepared and added to a conical flask. pH adjustments, if necessary, were made using 0.1 N NaOH or 0.1 N HCl. A measured quantity of CMC-SA-β-CD/NCO was then added, and the mixture was magnetically stirred until equilibrium was achieved. Subsequently, the CMC-SA-β-CD/NCO composite was separated from the dye solution, and the concentration of dye after adsorption (C_e) was determined from the UV–Vis absorbance spectrum. For highly concentrated MG solutions, dilution with distilled water preceded UV–Vis analysis to calculate the original concentration using the dilution factor.

To investigate the influence of various parameters, one parameter (such as *t*, *T*, initial MG concentration (C_o), CMC-SA-β-CD/NCO dosage (*m*), pH, or salt concentration) was varied while keeping all others constant. The concentration of MG before and after adsorption was quantified using a calibration curve based on absorbance at $\lambda_{max} = 617$ nm versus concentration. pH was varied from 3 to 10, with other parameters held constant ($T = 27$ °C, $t = 900$ min, $V = 40$ mL, $C_o = 50$ ppm, $m = 10$ mg); CMC-SA-β-CD/NCO dosage was varied from 5 to 100 mg at pH 5.5 ($T = 31$ °C, $t = 900$ min, $V = 40$ mL, $C_o = 50$ ppm); initial MG concentration ranged from 5 to 75 ppm at pH 5.5 ($T = 32$ °C, $t = 900$ min, $V = 40$ mL, $m = 20$ mg); contact time was studied from 5 to 300 min at pH 5.5 ($T = 32$ °C, $C_o =$ 40 ppm, $V = 40$ mL, $m = 20$ mg); and temperature was varied from 30 to 55 °C ($t = 170$ min, $C_o = 40$ ppm, $V = 40$ mL, $m = 20$ mg, pH = 5.5). To assess the effect of salts, 40 mL solutions of 40 ppm MG dye with varying salt concentrations were prepared, to which 20 mg of the composite was added under magnetic stirring ($T = 31$ °C, $t = 170$ min). After 170 min, the solution's concentration was analyzed

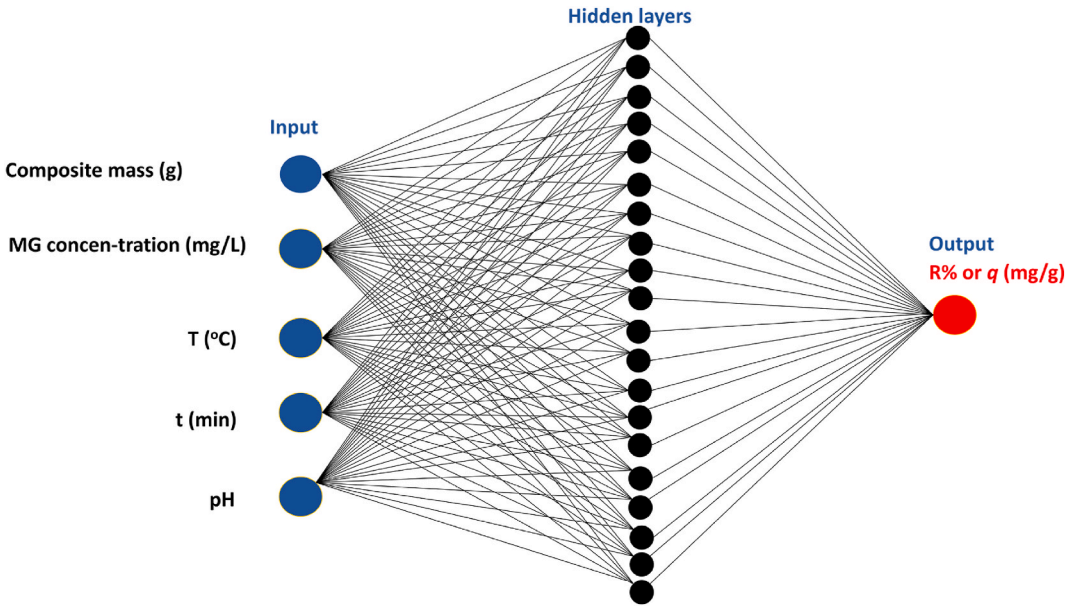

Fig. 1. Representation of ANN architecture (5 input-20 hidden layer-1 output).

using UV–Vis.

The data on MG dye concentration variations were used for isotherm studies, contact time effects for kinetics investigations, and temperature variations for thermodynamic studies, maintaining a constant temperature using a water bath. For the contact time investigation, small volumes of the MG solution were sampled at intervals between 5 and 300 min, and their absorbance measured using UV–Vis to calculate specific time concentrations. Results were duplicated for reproducibility.

For, NCO dose optimization reported in section 3.5.1, the adsorption investigations for CR removal were conducted at $T = 31$ °C, t = 900 min, with 50 ppm CR solution in 40 mL solution containing 10 mg CMC-SA-β-CD/NCO. Likewise, adsorption investigations for Bisphenol A (BPA) removal were performed at $T = 31$ °C, $t = 900$ min, with 40 mL, 32 ppm BPA solution containing 10 mg CMC-SA-β-CD/NCO. Optimization of composites for MG followed conditions of $T = 31$ °C, $t = 900$ min, $V = 40$ mL, $C_o = 50$ ppm, and $m = 10$ mg.

The adsorption capacity (q_e) and removal efficiency ($R\%$) of the CMC-SA-β-CD/NCO composite were calculated using experimental data in Eq. (1) and Eq. (2).

$$q_e = \frac{(C_o - C_e) \times V}{m} \tag{1}$$

$$R\% = \frac{(C_o - C_e)}{C_o} \times 100\% \tag{2}$$

Where C_e = concentration of MG after the adsorption equilibrium was established, C_o = initial concentration of MG in mg L^{-1}, V = volume of MG feed solution (L), and m = grams of CMC-SA-β-CD/NCO added into the MG solution. The higher value of $R\%$ and q_e indicates the higher effectiveness of CMC-SA-β-CD/NCO for MG decontamination.

2.7. Artificial neural networks (ANN)

ANN is a machine learning process consisting of a neuron-like network structure. It consists of output layers, input layers, and hidden layers. Through learning and connecting weights, a computer program creates a model by identifying the trends found within a set of inputs [28,33–35]. With the right training technique, this attribute enables the ANN to explain complex multivariate functions without doing extensive work. Hence, ANN provides a reliable interpretation by identifying complex non-linear patterns within a short period [33,36,37]. The hidden layer is in charge of taking data from the inputs and using it to forecast the result. The number of hidden layers that are employed will fluctuate depending on how complicated the architecture is [37]. The ANN architecture of the present study is given in Fig. 1. ANN architecture for this work consists of five inputs (i.e., CMC-SA-β-CD/NCO mass, Dye concentration, Temperature, time, and pH), 20 hidden layers in case of $R\%$ output and 15 hidden layers in case of adsorption capacity output, and one output layer (i.e, adsorption capacity (q) or $R\%$. The relationship between the experimental dataset and ANN is fundamental. The dataset serves as the cornerstone from which the ANN learns intricate relationships between inputs and outputs. By training on the experimental dataset, the ANN identifies and comprehends complex correlations among these parameters. This empirical foundation is essential for the training of any ANN model. Once trained on this dataset, the ANN can predict various outputs based on new input values. This enables rapid forecasting of estimated outcomes under specific experimental conditions. Notably, the dataset consisting of

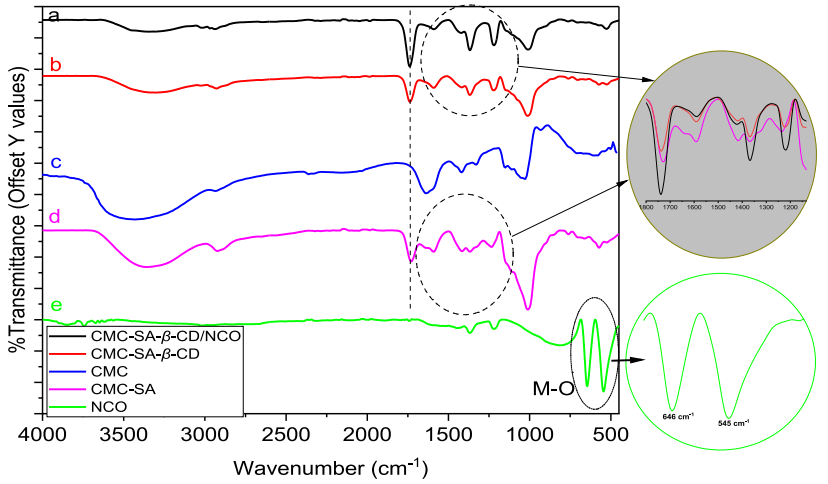

Fig. 2. FTIR spectrum of a: CMC-SA-β-CD/NCO, b: CMC-SA-β-CD, c: CMC, d: CMC-SA, and e: NCO.

Table 1
Comparison of characteristic FTIR stretching vibrations of $NiCo_2O_4$.

Preparation method	FTIR peaks (M − O stretching vibration) cm^{-1}	Ref.
Bottle guard extract assisted co-precipitation method	545 and 646	Present work
Hydrothermal	550 and 650	[39]
Hydrothermal	552 and 650	[38]
Co-precipitation method	553 and 658	[40]

30 experimental sets is partitioned into 15 % for validation, 70 % for training, and 15 % for testing. This division ensures effective learning, validates accuracy, and enhances the ANN's ability to generalize predictive capabilities.

[28,34]. The data was trained using MATLAB® R2022b using nftool. The experimental dataset was trained to achieve an R-value close to one, with a minimal mean square error (Eq. (3)) [37]. The regression plots and other supporting data are provided in the supplementary file.

$$MSE = \frac{1}{N}\sum_{i=1}^{N}\left(\left|y_{pred,i} - y_{exp,i}\right|\right)^2 \tag{3}$$

Where N, y_{pred}, y_{exp}, and y_m represent the total count of units, forecasted value, experimental value, and average of the experimental values [34].

3. Result and discussion

3.1. FTIR

The FTIR spectrum confirms the formation of $NiCo_2O_4$ (see Fig. 2). In the FTIR spectrum of NCO, two characteristic peaks between 400 and 1000 cm^{-1} were observed. The peak at 545 cm^{-1} and 646 cm^{-1} arises due to M − O (Ni–O and Co–O) stretching in tetrahedral and octahedral sites [38,39]. In previous studies, the M − O stretching peaks for NCO were reported at 650 and 550 cm^{-1} (nanorods) [39], 552 and 650 cm^{-1} (nanosheets) [38], 553 and 658 cm^{-1} (hexagonal microstructure) [40] by various researchers (Table-1). These values closely align with the peaks observed in this work, confirming that they are indeed attributed to the Ni–O and Co–O stretching vibrations.

CMC exhibits a broad peak between 3700 and 3000 cm^{-1} at 3448 cm^{-1} arises due to the hydroxyl-OH stretching vibration and the peak at 2931 cm^{-1} corresponds to the C–H stretching vibration [16,19–21,26,41]. The peak at 1600–1700 cm^{-1} corresponds to the carboxylate (COO^{1-}) stretching vibrations [16,19–21,26]. The peak at 1419 cm^{-1} is attributed to the other carboxylate stretching vibration [19,41]. The other major peaks like 1327 and 1026 cm^{-1} were reported to arise due to various C–O/C–*O*–C/O–H vibrations as reported in various studies [16,19,26,41]. In CMC-SA, the peak corresponding to O–H stretching vibrations was downshifted to 3358 cm^{-1} compared to CMC, indicating an interaction between CMC and SA (due to the chemical interaction of –OH groups in CMC and –COOH groups in SA). The appearance of an additional peak at 1729 cm^{-1} confirms that the reaction between –OH of CMC and –COOH of SA has successfully taken place, forming an ester linkage. This finding is in accord with previous literature, where cross-linking of bio polysaccharides resulted in the formation of additional peaks due to C═O stretching [42,43]. Both CMC-SA-β-CD and CMC-SA-β-CD/NCO exhibit similar peaks to those of CMC-SA except for some shifting and pattern of appearance of these peaks

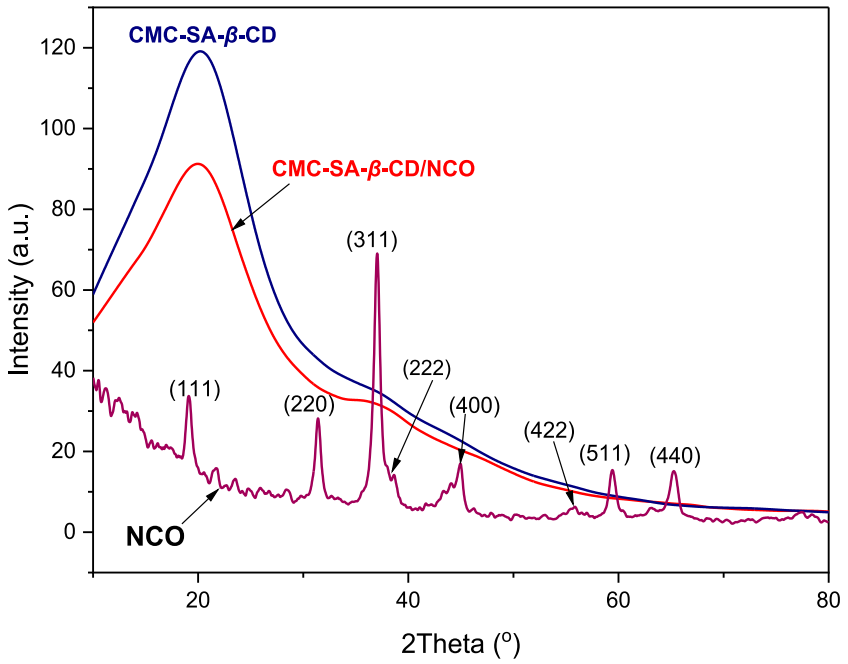

Fig. 3. XRD patterns CMC-SA-β-CD/NCO, CMC-SA-β-CD, and (b) NCO.

between 1800 and 1200 cm^{-1}. The peak corresponding to O–H stretching vibration appears at 3305 cm^{-1} for CMC-SA-β-CD and at 3347 cm^{-1} for CMC-SA-β-CD/NCO. Both of these were downshifted compared to CMC-SA. The peak corresponding to C–H stretching vibration was slightly up-shifted to 2928 and 2939 cm^{-1} for CMC-SA-β-CD and CMC-SA-β-CD/NCO, respectively. Similarly, the shifting in the peak corresponding to C═O stretching was observed. For both CMC-SA-β-CD/NCO and CMC-SA-β-CD the peak at 1737 cm^{-1}, was 8 cm^{-1} up-shifted compared to CMC-SA peak. No major shifting occurs between 1300 and 1700 cm^{-1} region. From the results, it is concluded that β-CD is successfully linked to CMC through succinic acid. As for CMC-SA-β-CD/NCO, overall peaks are the same as those observed for CMC-SA-β-CD. No sharp M − O stretching peaks between 400 and 700 cm^{-1} were observed. This could be due to the overlapping of peaks of CMC-SA-β-CD and NCO in that region as well as the very low quantity of NCO in the composite. Hence, based on the IR spectrum alone, the presence of NCO in the composite material cannot be confirmed. Only shifting in the O–H stretching and C–H stretching peaks was observed when comparing the spectrum of CMC-SA-β-CD and CMC-SA-β-CD/NCO. In the composite, there is no evidence of chemical bonding between NCO and the polymer matrix; rather, there are predominantly weak interactions that secure the nano reinforcement within the polymer matrix. Plausible interactions between NCO and CMC-SA-β-CD include van der Waals forces and hydrogen bonding. Specifically, hydrogen bonding may occur between the oxygen atoms in NCO and the hydrogen atoms from the hydroxyl (–OH) and carboxylic acid (–COOH) groups present in the CMC-SA-β-CD matrix.

3.2. Powder XRD

NCO exhibits eight sharp peaks in powder XRD diffractogram (see Fig. 3). The peak at $2\theta = 19.1°, 31.4°, 37.1°, 38.6°, 45.0°, 55.7°, 59.4°$, and $65.3°$ corresponds to (111), (220), (311), (222), (400), (422), (511), and (440) planes, respectively (PDF#00-020-0781). NCO belongs to the cubic crystal system and F*3 space group with $a = b = c = 8.05$ Å and $\alpha = \beta = \gamma = 90^{o}$ angle (PANalyticalX'PertHighscore). The appearance of these peaks and the absence of the impurity peaks in the XRD diffractogram confirm the formation of $NiCo_2O_4$. Scherrer's equation ($D = 0.9\lambda/\beta.\cos\theta$) was used to calculate the crystalline size of the NCO. Where D, λ, β, and θ represent the crystalline size (nm), wavelength of Cu-Kα source (0.15406 nm), full-width-at-half maxima of highest intensity peak, and Bragg's angle ($2\theta/2$), respectively. The highest intensity peak (311) plane was chosen to calculate the crystalline size of the NCO. The crystalline size of NCO was found to be ~10 nm suggesting its nanocrystalline structure. The other parameters like cell constant, microstrain, X-ray density, and dislocation density are incorporated in the supplementary file.

CMC-SA-β-CD exhibits a broad peak along with a weak peak in the range of $2\theta = 10°$–$40°$. The initial peak is observed at $2\theta = \sim 20.2°$, and a secondary weak peak appears at $2\theta = \sim 36.3°$. Notably, this peak is observed in a comparable region for other polymers based on CMC and β-CD [20,26,41,44]. Similarly, one broad peak between the same region was observed for CMC-SA-β-CD/NCO. The appearance of the broad peaks suggests the amorphous nature of both, CMC-SA-β-CD and CMC-SA-β-CD/NCO. After NCO reinforcement, the first peak appears at 20.0°, and the second at 37.1°, slightly shifted compared to pure CMC-SA-β-CD. A slight peak enhancement near the (311) plane of the NCO in the CMC-SA-β-CD/NCO composite was observed. No sharp peaks corresponding to pure NCO were observed in the nanocomposite, likely due to the larger quantity of CMC-SA-β-CD polymer compared to NCO in the composite. However, a notable change indicating the presence of NCO is observed in CMC-SA-β-CD/NCO, which exhibits a less broad

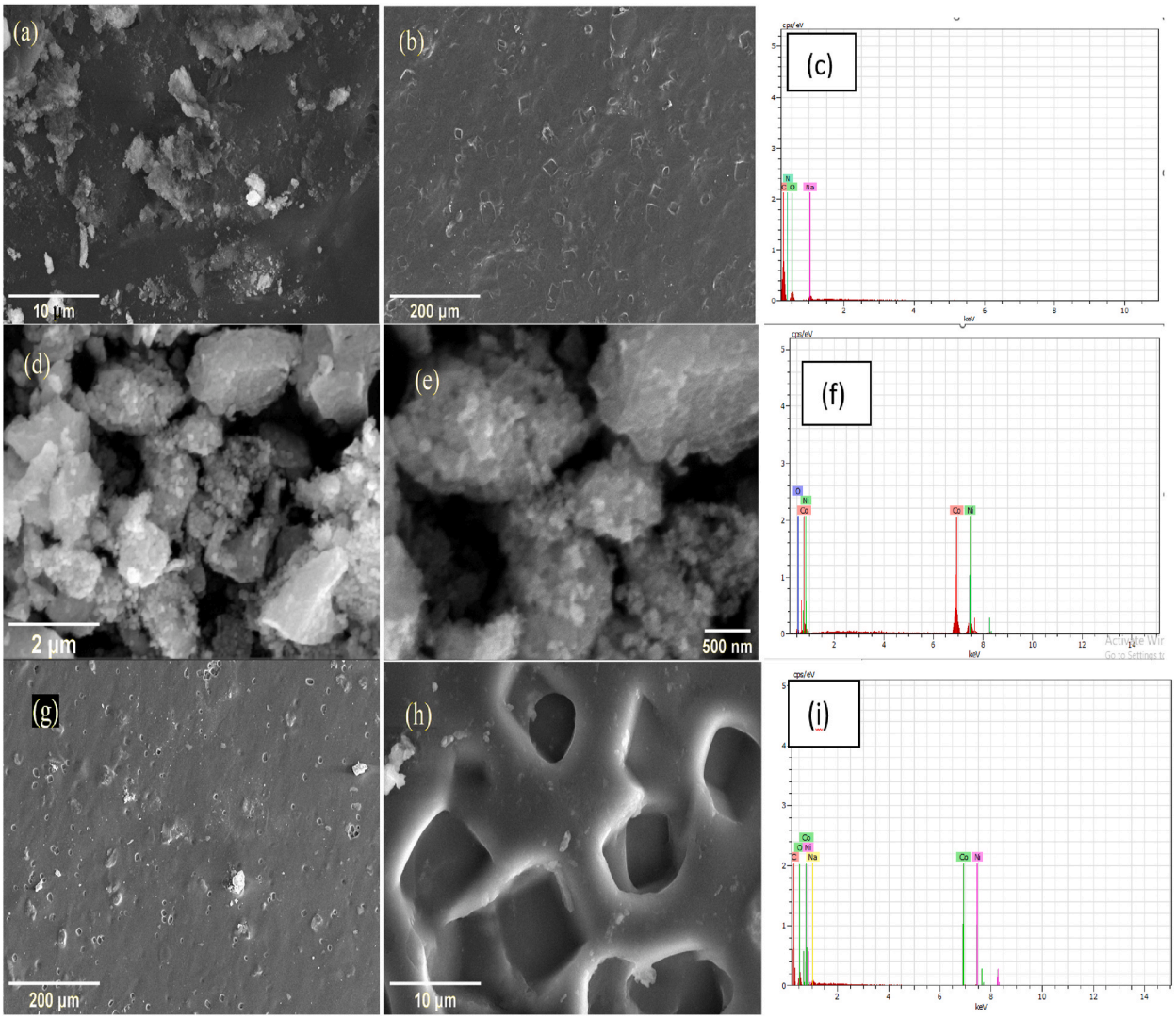

Fig. 4. SEM images and EDS spectrum of CMC-SA-*β*-CD (a–c), NCO (d–f), and CMC-SA-*β*-CD/NCO (g–i).

peak than CMC-SA-*β*-CD. The incorporation of more crystalline NCO in the CMC-SA-*β-CD* results in a composite with increased crystallinity compared to native CMC-SA-*β*-CD. A similar observation was made in the previous work [44].

3.3. Surface investigations

SEM is a crucial technique for investigating composite adsorbents, as their surface properties play a vital role in determining their adsorption performance. SEM images provide detailed insights into the surface morphology, including the presence of pores, reinforcement such as NCO in the CMC-SA-*β*-CD matrix, and whether the surface exhibits a layered or smooth structure. These factors significantly impact the adsorption efficiency of an adsorbent. Furthermore, SEM, in conjunction with EDS, serves to confirm the formation of the nanocomposite CMC-SA-*β*-CD/NCO. CMC-SA-*β*-CD does not exhibit any definite shape (Fig. 4-a) but a large number of octahedrons like shallow pits were visible on the surface (Fig. 4-b). The size of the shallow octahedron pits is not consistent. The largest octahedron pit measures 41.3 µm in length and 32.9 µm in width. The smaller ones measure 8.1 µm in length and 6.5 µm in width. However, the width: length ratio was consistent (i.e., ~1:1.25). These pits may help to accumulate adsorbate molecules and expose more surface for the adsorbent-adsorbate interaction. The EDS analysis (Fig. 4-c) suggests that in addition to C, O, and Na small amount of N element impurity was present in CMC-SA-*β*-CD. Owing to the nanosize, the nanomaterial tends to agglomerate. Spherical particles of NCO aggregate to form irregular oval shaped clusters (see Fig. 4-d and 4-e). The most prevalent particle size of NCO was measured between 60 and 70 nm (measured randomly using Image J software). The EDS spectrum of NCO (Fig. 4-f) confirms the presence of Ni and Co. The ratio of the atom percentage of Ni:Co was 1.0:2.09, which was closer to the 1:2 ratio. Hence, confirmation of the formation of nanocrystalline and nanosize NiCo2O4 was obtained from XRD, SEM, and EDS analyses. The nanocomposite CMC-SA-*β*-CD/NCO

Table 2
Surface area, pore size, and pore volume of CMC-SA-β-CD and CMC-SA-β-CD/NCO.

Surface property	CMC-SA-β-CD	CMC-SA-β-CD/NCO
BET surface area (m^2/g)	2.16	0.798
Pore size (Å)	39.135/22.941	124.463/41.621
Pore volume (cm^3/g)	0.001239	0.000848

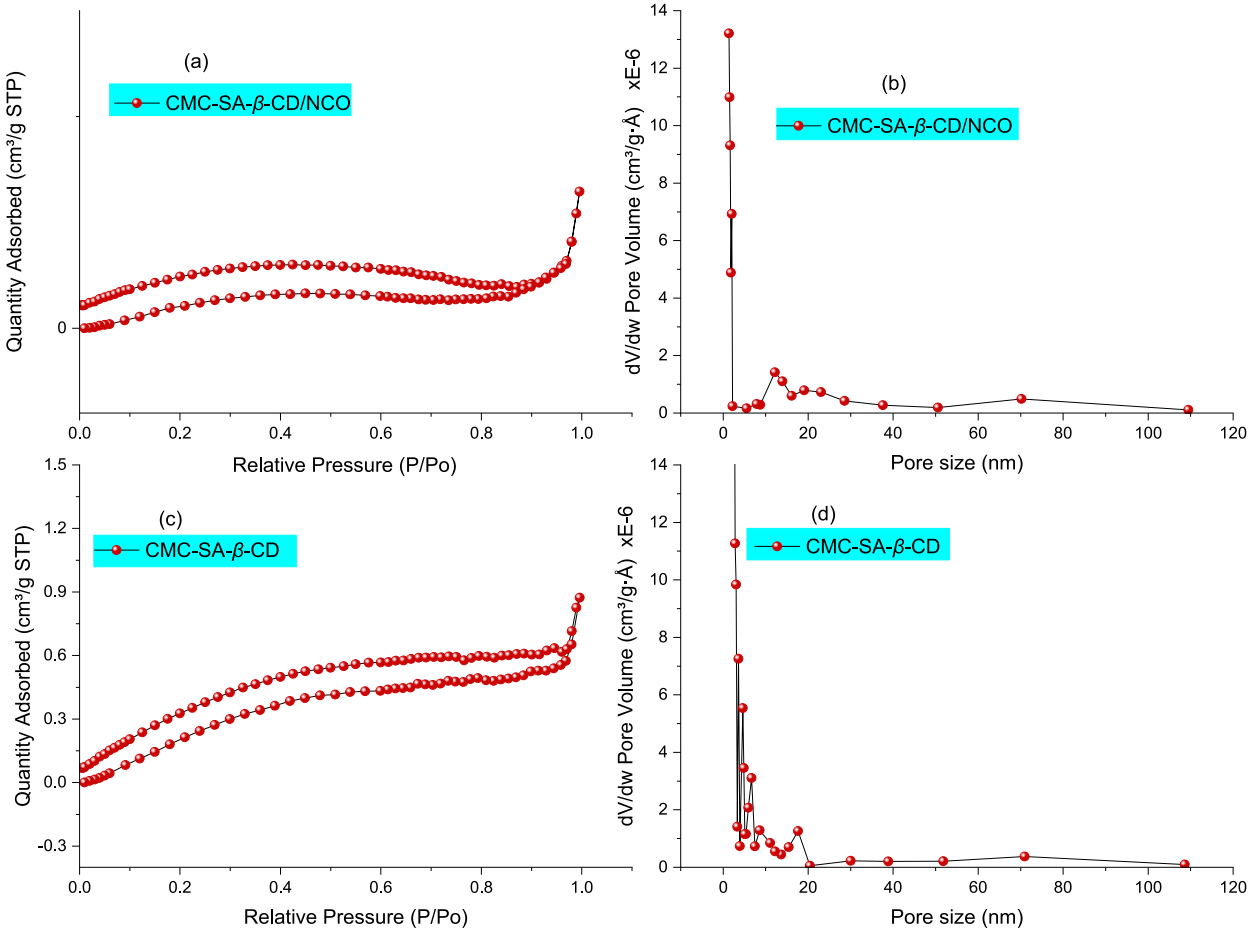

Fig. 5. N_2 adsorption-desorption isotherm (a, c) and BJH pore size distribution (b,d) of CMC-SA-β-CD and CMC-SA-β-CD/NCO.

(Fig. 4-g and 4-h) exhibited a surface having a deeper cavity than CMC-SA-β-CD. The most prevalent shape of the cavity was an octahedron with the appearance of some ovule shaped and square shaped cavities. The length and width of the cavity fall below 10 μm for most cavities. Therefore, with the reinforcement of NCO in CMC-SA-β-CD, the cavities become more uniform, smaller, and deeper than in CMC-SA-β-CD. This can provide better adsorption. The EDS spectrum of the composite (Fig. 4-i) confirms the presence of NCO in the composite, thereby, confirming the formation of the CMC-SA-β-CD/NCO.

The BET surface area analysis suggests the porous nature of the material due to the generation of the hysteresis loop. The BET surface area and pore volume of CMC-SA-β-CD were higher than those of CMC-SA-β-CD/NCO (see Table 2), possibly attributed to the occupation of some adsorption sites by NCO. The average pore size for both CMC-SA-β-CD and CMC-SA-β-CD/NCO falls between 2 and 50 nm, hence, both the native CMC-SA-β-CD and its composite indicate the presence of mesopores (>50 nm = macroporous; <2 nm = microporous; 2–50 nm = mesoporous). Moreover, the pore size of CMC-SA-β-CD was increased after the NCO reinforcement. Although the adsorption-desorption curve does not close at $P/P_0 = 0$ in the N_2 adsorption-desorption curve (Fig. 5), the possible explanation could be that after adsorption some sites may have become inaccessible to the adsorbate molecules creating a trap within the adsorbent surface [45]. Hence, a very slow desorption or negligible desorption takes place in those cases leading to an open hysteresis loop [45]. Both materials exhibit a type II-like isotherm with H3/H4 type hysteresis loop which is often observed for slit-type pores. Both materials exhibited a broad pore size distribution.

The zeta potential at different pH (Fig. S2) suggested that the synthesized polymer and its' nanocomposite material exhibit a

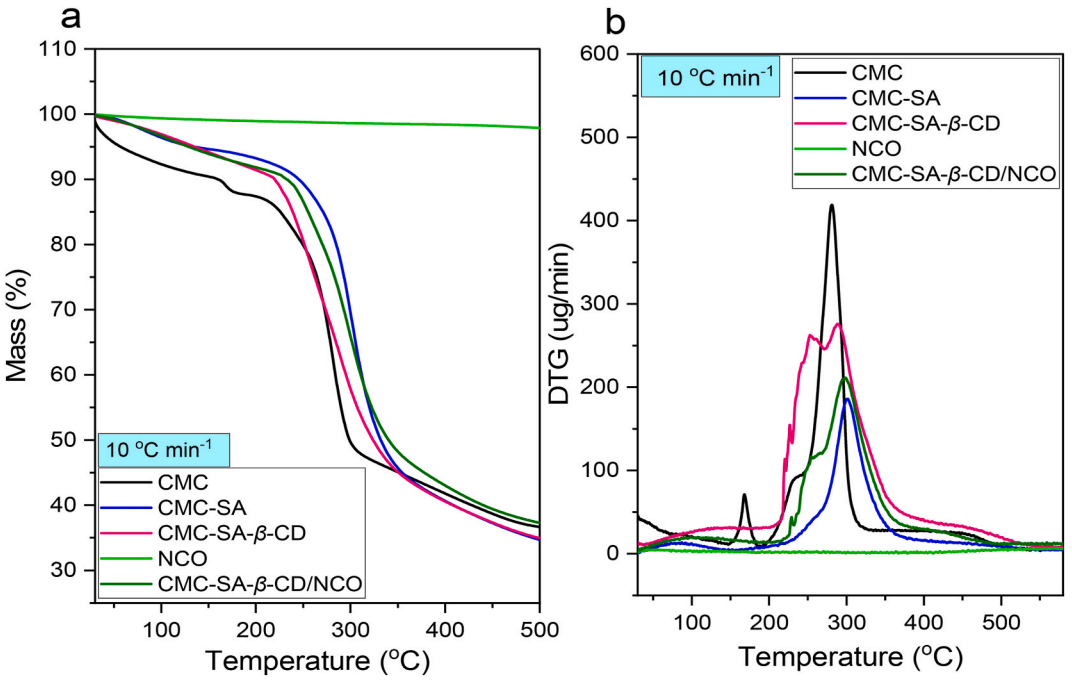

Fig. 6. TG (a) and DTG (b) graph of CMC, NCO, CMC-SA, CMC-SA-β-CD and CMC-SA-β-CD/NCO.

negative surface between pH 3–9, a similar negative zeta potential was observed for functionally modified cellulose nanofiber (FMCSN) [46]. The CMC-SA-β-CD/NCO composite exhibits a slightly positive surface at pH = ~2, whereas the CMC-SA- β-CD possesses a negative surface at a similar pH. The point of zero charge (*p*Hpzc) of CMC-SA-β-CD was observed around 2 pH and that of CMC-SA-β-CD/NCO was not observed between pH = 2–9 and hence, it must exist below pH < 2.

The negative surface indicates the presence of carboxylate and hydroxyl groups on the polymer and its composite's surface. These values indicated that both CMC-SA-β-CD and CMC-SA-β-CD/NCO can enhance the adsorption of cationic chemical species. The particle size distribution (see supplementary file) indicates that CMC-SA-β-CD/NCO exhibited a broader particle size distribution compared to CMC-SA-β-CD. The presence of smaller particles (2–3.5 μm) in CMC-SA-β-CD/NCO may have arisen due to the reinforcement of NCO (mean particle size of NCO = 0.4 nm obtained using particle size analysis).

3.4. Thermal stability

Thermal analysis is crucial for evaluating the thermal stability of materials, particularly adsorbents. It ensures that the adsorbent remains stable and does not decompose during its application under various temperatures. Thermal stability is vital because if the adsorbent undergoes decomposition at the operating temperatures studied, it could potentially contaminate the water and alter its adsorption capacity due to structural breakdown.

TG and DTG profile of samples is depicted in Fig. 6. NCO is stable over a wide range of temperatures (Fig. 6 (a)). Up to 590 °C, only 3.4 % mass loss was observed. Pristine CMC shows more than one decomposition peak in the DTG curve. The decomposition below 183 °C leads to a mass loss of ~12 % was attributed to the loss of water molecules adsorbed on the surface of CMC. The two peaks appear as a convoluted peak between 200 and 345 °C. These peaks are the major decomposition peaks and can be attributed to the decomposition of glucopyranose structure units in CMC. A total mass loss of ~42 % was observed during these decomposition stages. Thereafter, a slow decomposition was observed up to 590 °C with a mass loss of ~11 %. Therefore, CMC loses 65 % mass between 27 and 590 °C due to loss of water followed by decomposition. The polysaccharides often undergo dehydration, de-polymerization, and then decomposition leading to the formation of various gaseous products [47]. The reason for high mass loss during the decomposition could be attributed to the abundance of functional group (i.e., CH_2COO^{1-}) on CMC that may undergo decarboxylation forming CO and CO_2. Similarly, a large content of the CMC backbone undergoes decomposition due to depolymerization followed by decomposition [47,48]. It should be noted that following the second decomposition curve, a slow decomposition is observed, indicating the formation of a stable carbonaceous char intermediate due to the high carbon content in the CMC backbone. Therefore, thereafter, a slow decomposition ensues. The decomposition of CMC-SA was comparable to that of CMC. This could be due to major CMC structural features in CMC-SA. In CMC-SA a broad peak between 27 and 150 °C leading to 5.4 % mass loss could be attributed to loss of trapped gaseous, water, or other volatile impurities. The decomposition of CMC-SA commences at 209 °C. Between 209 and 301 °C, CMC-SA loses ~54 % mass. Subsequent decomposition leads to a total mass loss of ~68 % up to 590 °C.

Overall, the DTG profile of CMC-SA-β-CD and CMC-SA-β-CD/NCO does not differ much because of only a small amount of NCO

Table 3
TG and DTG peak profile data of the major decomposition event.

Sample	T_o (°C)	T_p (°C)	Mass loss (%)
CMC	203	280	42
CMC-SA	209	301	54
CMC-SA-β-CD	214	252; 289	48
CMC-SA-β-CD/NCO	218	298	46

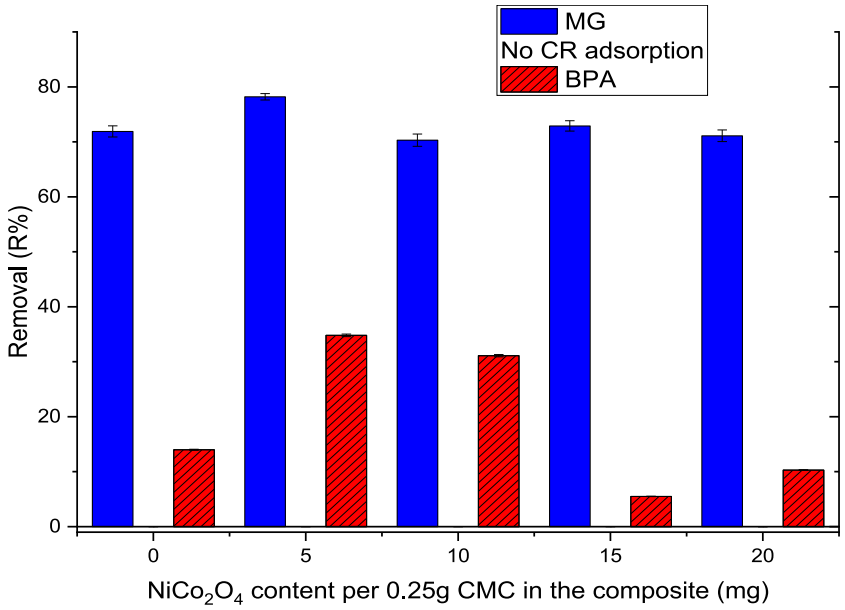

Fig. 7. Removal of MG, CR, and BPA using CMC-SA-β-CD/NCO (0, 5, 10, 15, and 20 mg).

filling. The mass loss of ~9 % below 213 °C due to the loss of volatile impurities and moisture was observed in both CMC-SA-β-CD and CMC-SA-β-CD/NCO. The higher mass loss observed below 200 °C indicates that both CMC-SA-β-CD and CMC-SA-β-CD/NCO contain a significant amount of physically adsorbed volatile materials and moisture, both on the surface and within the cavities. Therefore, it is essential to remove moisture from the composite before its application in adsorption processes to clear adsorption sites blocked by the pre-adsorbed moisture. This can be achieved by heating the composite; however, the temperature should be kept below its decomposition temperature to prevent structural degradation. The major decomposition event led to mass loss of 48 % and 46 % (Table 3) for CMC-SA-β-CD and CMC-SA-β-CD/NCO, respectively, followed by a slow decomposition leading to a total mass loss of 66–67 %. Both, the onset temperature (T_o) and the peak decomposition temperature (T_p) were increased in the case of the CMC-SA-β-CD/NCO. The result indicated that the incorporation of NCO enhances the thermal stability of the CMC-SA-β-CD. The details of the onset and peak decomposition temperature of the major decomposition event are provided in Table 3.

3.5. Effect of different parameters on the adsorption of MG

3.5.1. Effect of NCO dose

The effect of variation in mg dose of NCO reported in section 2.4 on the *R%* of MG is depicted in Fig. 7. All five adsorbents were found to exhibit good MG removal and very weak adsorption for BPA (*R%*<40 %) (Fig. 7). None of the materials adsorbed anionic CR dye. The results suggested that the composite surface may possess a negative charge, hindering the approach of anionic CR towards the nanocomposite surface (repulsion), and consequently, no adsorption occurs. Since BPA does not carry a charge, it can approach the negative composite surface without repulsion, leading to slight adsorption on the CMC-SA-β-CD/NCO's surface due to weaker interactions. The composite exhibits high adsorption for the cationic MG dye because of its negative surface, facilitating attraction between the adsorbate and adsorbent.

3.5.2. Effect of salts

The removal percentage of MG using CMC-SA-β-CD/NCO composite was studied by varying different parameters (see Fig. 8). The uptake MG on the composite surface in the presence NaCl, KCl, $CaCl_2$ and $MgCl_2.6H_2O$ (concentration = 0.005, 0.01, and 0.1 M, Fig. 8-a) was studied to understand the effect of monovalent and divalent salt on the adsorption. As depicted in Fig. 8-a, in the absence of salt, there was a high dye removal (*R%*>90 %). However, in the presence of even a small concentration of salt (0.005 M), the *R%* falls below

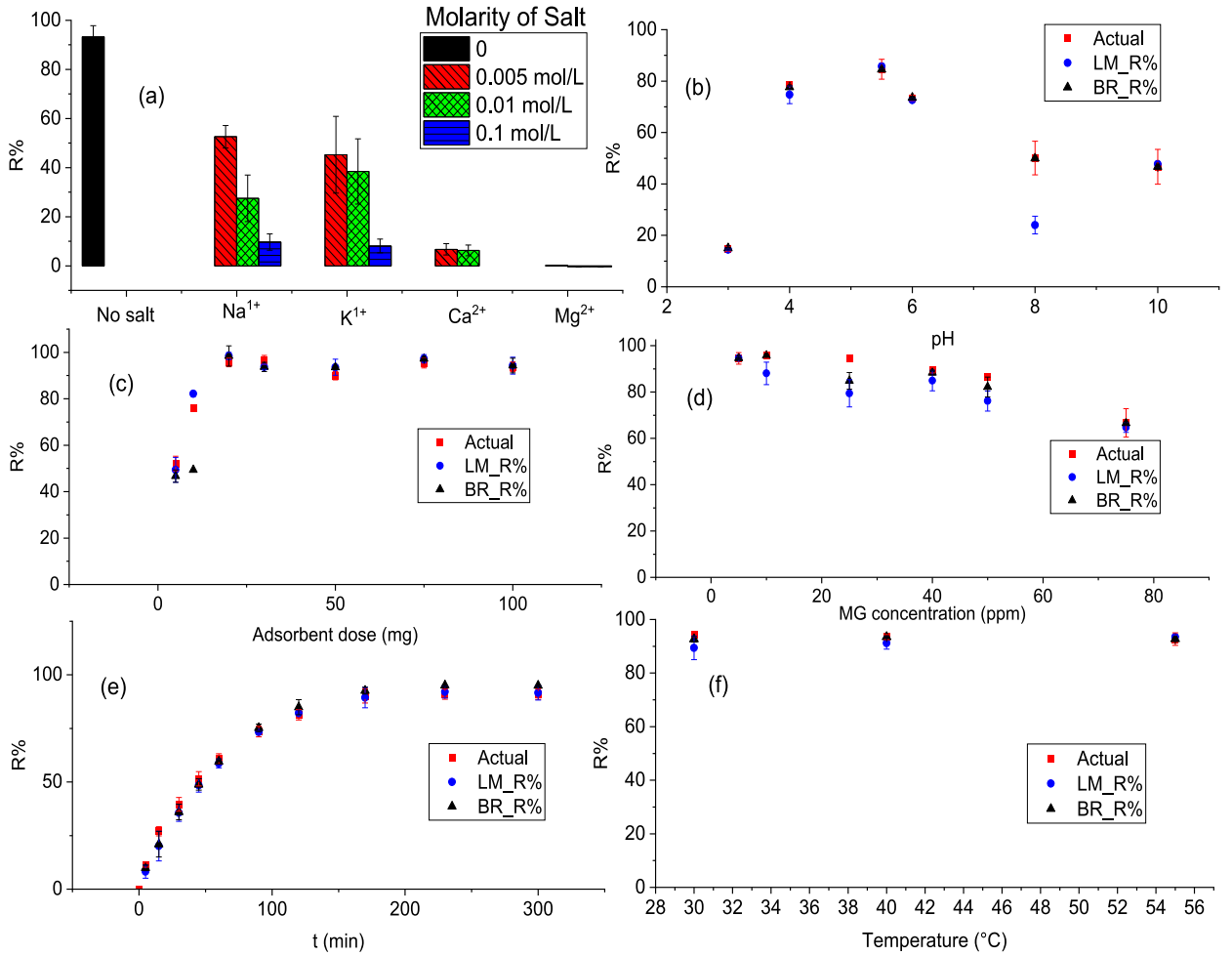

Fig. 8. Effect of various parameters on the adsorption of MG using CMC-SA-*β*-CD/NCO and their simulated values using ANN model Levenberg-Marquardt (LM) and BR (Bayesian regularization).

55 % for all salts. The major decline can be attributed to the competitive adsorption of metal ions on the CMC-SA-*β*-CD/NCO surface, occupying the active adsorption sites and hence, reducing the active sites available for MG adsorption. It was observed that at higher salt concentrations, the *R%* declines rapidly because of the occupation of a large number of adsorption sites on CMC-SA-*β*-CD/NCO leading to a greater decline in MG *R%*. Moreover, it was evident that the effect of divalent metal ions (Ca^{2+} and Mg^{2+}) was more drastic than monovalent metal ions (Na^{+} and K^{+}). This was because of more interaction between positive cation and negative composite surface. There was no significant change in the *R%* of MG within monovalent ions but when comparing divalent ions it was observed that the effect of Mg^{2+} was slightly more downward than Ca^{2+}. It should be noted that the mole ratio of Cl^{1-} in monovalent: divalent metal ions is 1:2 and hence, more decline in the *R%* of MG in the case of divalent salt could be associated with more Cl adsorption that may occupy weaker adsorption sites on CMC-SA-*β*-CD/NCO. In general, the order of MG *R%* was No salt > NaCl ≥ KCl > $CaCl_2$>$MgCl_2$. However, the effect of ionic salt on the *R%* of MG is not consistent when compared with previous literature, likely due to the different adsorbent materials used. For instance, k.Abbas and A.AL-Da'amy [49] observed a trend in MG *R%* as follows: $CaCl_2$>$MgCl_2$>KCl > NaCl. They reported that Even in the presence of a salt concentration of 0.02 M, the %R for MG remained higher than 80 % for all salts [49]. The significant reduction in the adsorption of MG onto CMC-SA-*β*-CD/NCO in the presence of salts suggests that electrostatic interactions between the adsorbate and adsorbent play a crucial role in influencing the adsorption of MG.

3.5.3. Effect of pH

The *R%* of MG (Fig. 8-b) was increased up to 5.5 pH (*R%*>84 %; No pH variation using HCl or NaOH) and declined after that. Under very acidic (pH~3) and basic conditions (pH = 8 and 10), the *R%* of MG was below 50 %. At pH = 4, 5.5, and 6, the *R%* was between 70 and 85 %. The higher adsorption in the pH 4–6 may be due to cationic-anionic attraction between the dye molecule and CMC-SA-*β*-CD/NCO's surface. Nevertheless, as previously examined, it becomes apparent that the *R%* of MG is significantly influenced by the presence of ionic species. Consequently, the observed reduction in the *R%* of MG, whether with an increase or decrease in pH, could be attributed to the competitive adsorption of ions from NaOH and HCl (see section 3.5.2), used for pH adjustment, alongside dye

molecules. Sometime if proper measurements are not taken then fading in dye color because of structural changes at high pH can be mistaken for adsorption. MG forms a carbinol base at higher pH levels; therefore, it is also conceivable that the decline observed was due to reduced interaction between the carbinol base form of MG and the surface of CMC-SA-*β*-CD/NCO [50].

3.5.4. Effect of CMC-SA-*β*-CD/NCO amount

Increasing the CMC-SA-*β*-CD/NCO dosage from 5 mg to 20 mg resulted in a notable rise in the removal efficiency (*R%*) for MG, escalating from 49 % to 97 % (Fig. 8-c). This enhancement can be attributed to the increased availability of active sites for adsorption, stemming from the higher content of the adsorbent. Within the range of 20 mg–100 mg of CMC-SA-*β*-CD/NCO dosage, minimal variation is observed in the *R%* of MG. This suggests that the maximum adsorption capacity of MG on CMC-SA-*β*-CD/NCO has been attained, and equilibrium has been established. Consequently, further increments in the adsorbent dosage do not significantly impact the removal of MG from the solution. Moreover, for a consistent *R%*, the mass of MG adsorbed remains constant. Therefore, increasing the CMC-SA-*β*-CD/NCO dose results in a reduction in adsorption capacity (mg of MG per g of CMC-SA-*β*-CD/NCO) [28].

3.5.5. Effect of MG concentration

The effect of MG solution concentration on the *R%* is depicted in Fig. 8-d. The *R%* for MG remains above 90 % for 5, 10, and 25 ppm MG solution. The *R%* drops continuously at higher concentrations>25 ppm. However, at an MG concentration of 40 ppm, the composite demonstrates a good removal percentage (*%R*) and adsorption capacity for MG. At 75 ppm MG dose, the *R%* declined to 65 %. This decline was due to the saturation of adsorption sites on CMC-SA-*β*-CD/NCO. The adsorption sites on CMC-SA-*β*-CD/NCO were already occupied by the MG dye molecules and a further increase in the MG concentration resulted in more MG molecules in the solution than on the surface of CMC-SA-*β*-CD/NCO, leading to declined *R%*. The data was fitted to various isotherm models to calculate maximum adsorption capacity (section 3.6).

3.5.6. Effect of time

The adsorption process of MG onto CMC-SA-*β*-CD/NCO exhibited a gradual pace, as depicted in Fig. 8-e. A steady increase in removal efficiency (*R%*) was observed up to 170 min, signifying the establishment of equilibrium at this point. After a 60-min contact between CMC-SA-*β*-CD/NCO and the MG solution, a 59 % removal was achieved. Subsequently, from 170 min onwards, additional contact times (230 min and 300 min) did not significantly influence the adsorption of MG onto CMC-SA-*β*-CD/NCO. While the initial adsorption was relatively faster, the subsequent time required to attain equilibrium proved to be a gradual process. Almost twice the time was necessary to achieve the removal of nearly half of the initial *R%* of MG compared to the first hour. To gain insights into the kinetics of the adsorption process, the data was subjected to fitting with various kinetic models (section 3.7).

3.5.7. Effect of temperature

The *R%* of MG onto CMC-SA-*β*-CD/NCO has a negative relation between *R%* and temperature (Fig. 8-f). The results suggested the adsorption process was exothermic. At higher temperatures, MG molecules can get desorbed from the composite surface resulting in decreased *R%*. However, the variation in *R%* was not drastic. i.e., the change in the *R%* by changing the temperature by 15 °C was lower than 2 %.

3.5.8. ANN training

A regression plot is a useful tool for evaluating the performance of an ANN regression model. It illustrates how expected values align with actual results (linear line), providing insights into the model's efficiency and suggesting possible areas for improvement (see supplementary file). From the regression plots (Figs. S4, S6, S8, and S9), it was evident that the ANN-predicted values showed a better fit for the adsorption capacity output than for the *R%* output, which is also corroborated by Fig. S12. There was a greater spread of data points for the *R%* output predicted using either the BR or LM algorithm, indicating that these algorithms are less reliable for predicting *R%* output. The performance plots (Figs. S5 and S7) for the training, validation, and test sets show the mean squared error (MSE) of the network over training epochs, illustrating the evolution of the network's learning process. A decrease in MSE for the training set indicates successful learning from the training data. The best performance is observed as the lowest MSE value. As shown in Figs. S5 and S7, the LM algorithm is faster than the BR algorithm. The corresponding MSE and R values are reported in the supplementary file (Table S2). The ANN was effectively trained using the experimental dataset to accurately predict the adsorption capacity and estimate the removal efficiency (%) for MG uptake using CMC-SA-β-CD/NCO. This model can handle new inputs encompassing varying conditions such as pH, temperature, time (t), composite mass, and MG concentration.

3.6. Isotherm

The various equations (Eq. 3-10) were used to evaluate the isotherm parameters for the adsorption of MG onto CMC-SA-*β*-CD/NCO. Eq. (4) is the non-linear Freundlich equation and the corresponding linear form is Eq. (5). It assumes multilayer adsorption on a heterogenous adsorbent surface. Eq. (6) is the Langmuir equation and it assumes that intermolecular forces are stronger at least distance. Hence, monolayer adsorption on homogenous adsorbent surfaces is assumed [51,52]. Eq. (7) and Eq. (8) corresponds to Temkin and Dubinin–Radushkevich (D-R) isotherm, respectively. Temkin isotherm assumes a uniform distribution on heterogenous sites and binding energy varies linearly over these sites [53]. D-R isotherm is mostly applicable to the adsorption of gas onto carbons with uniform micropores [54].

Table 4
Isotherm parameters for the adsorption of MG onto CMC-SA-β-CD/NCO using experimental and ANN predicted data.

Model	Parameter	MG	LM	BR
Langmuir	q_m (mg g^{-1})	182 ± 4	180 ± 1	218 ± 5
	K_L (L mg^{-1})	0.593 ± 0.060	0.470 ± 0.085	0.410 ± 0.026
	R^2	0.998	0.985	0.998
Freundlich	K_F (mg. g^{-1}(L $mg^{-1})^{1/n}$)	52.3 ± 8.1	53.4 ± 6.1	52.6 ± 7.4
	$1/n$	0.496 ± 0.097	0.425 ± 0.069	0.524 ± 0.087
	R^2	0.835	0.903	0.900
Temkin	A_T (L g^{-1})	7.90 ± 0.26	9.06 ± 0.46	6.42 ± 0.02
	b_T (kJ mol^{-1})	71.4 ± 5.9	82.2 ± 7.2	62.7 ± 1.3
	R^2	0.961	0.982	0.999
Dubinin–Radushkevich	q_m (mol g^{-1})	(1.17 ± 0.42)E−3	(0.76 ± 0.21)E−3	(1.38 ± 0.46)E−3
	δ (mol^2 J^2)	(3.87 ± 0.62)E−9	(3.29 ± 0.44)E−9	(4.07 ± 0.55)E−9
	E (kJ mol^{-1})	11.4 ± 0.8	12.3 ± 0.8	11.1 ± 0.7
	R^2	0.884	0.932	0.933

$$q_e = K_F C_e^{\frac{1}{n}} \quad \text{Non-Linear Freundlich equation} \tag{4}$$

$$\log q_e = \log K_F + \frac{1}{n}\log C_e \text{ Linear form of the Freundlich isotherm} \tag{5}$$

$$\frac{C_e}{q_e} = \frac{1}{q_m}C_e + \frac{1}{K_L q_m} \text{ Langmuir isotherm} \tag{6}$$

$$q_e = B_1 \ln A_T + B_1 \ln C_e \text{ Temkin isotherm} \tag{7}$$

$$\ln q_e = \ln q_m - \delta\varepsilon^2 \text{ D-R isotherm} \tag{8}$$

Where K_F=Freundlich constant; K_L=Langmuir's constant; B_1=(RT/b_T) = Temkin constant; b_T = Another Temkin constant related to heat; R=Universal gas constant; T = temperature at which adsorption was performed; $1/n$ = heterogeneity facto; q_m = Langmuir maximum adsorption capacity of the composite for MG removal; ε = Polanyi potential (Eq. (9)); δ = constant associated with the adsorption energy. The D-R isotherm allows the calculation of adsorption energy using Eq. (10). The separation factor (R_L, eq. (11)) is also an important parameter to identify the favourability of the adsorption process which can be calculated using K_L.

$$\varepsilon = RT \ln\left(\frac{C_s}{C_e}\right) \tag{9}$$

$$E = \frac{1}{\sqrt{2\delta}} \tag{10}$$

$$R_L = \frac{1}{1 + K_L C_0} \tag{11}$$

Where C_s = the saturation MG concentration.

The isotherm parameters for the adsorption of MG onto CMC-SA-β-CD/NCO are depicted in Table 4. The corresponding plots for isotherm and kinetic models are given in Fig. S10. The closer to 1 value of R^2 indicates the best suited method to describe the adsorption of MG onto CMC-SA-β-CD/NCO. The linear relationship was not obtained for Freundlich and Dubinin–Radushkevich plots (Supplementary file) as indicated by poor R^2 value. Somehow, a near linear plot was obtained for the Temkin model, but the value of the linear regression coefficient was still lower than 0.99 to produce accurate calculations. The best fit was observed for the Langmuir isotherm. This suggests that the adsorption of MG onto CMC-SA-β-CD/NCO was governed by single layer adsorption of MG onto identical adsorption sites on the composite surface. The Langmuir maximum adsorption capacity indicates that 182 ± 4 mg MG was absorbed onto 1 g CMC-SA-β-CD/NCO composite. The value of R_L was 0.277, 0.161, 0.0712, 0.0457, 0.0369, and 0.0249 for MG initial concentrations 5, 10, 25, 40, 50, and 75 mg L^{-1}, respectively. If the value of R_L is 0, 1, greater than 1, or between zero and one, it suggests irreversible, linear, non-favorable, and favorable adsorption conditions. As the value of R_L for all studied MG solutions was between 0 and 1, the adsorption of MG onto the CMC-SA-β-CD/NCO composite was favorable. The adsorption energy can provide useful information about the adsorption being physisorption (Energy <8 kJ mol^{-1}) or chemisorption (Energy >8 kJ mol^{-1}). The approximate activation energy calculated from the Dubinin–Radushkevich method was higher than 8 kJ mol^{-1}, suggesting that probably, the adsorption of MG onto the composite surface was governed by chemical adsorption. Chemisorption requires high energy due to stronger adsorbent-adsorbate interaction forces than physisorption. Therefore, the calculated adsorption energy and Langmuir point towards the chemisorption of MG onto CMC-SA-β-CD/NCO.

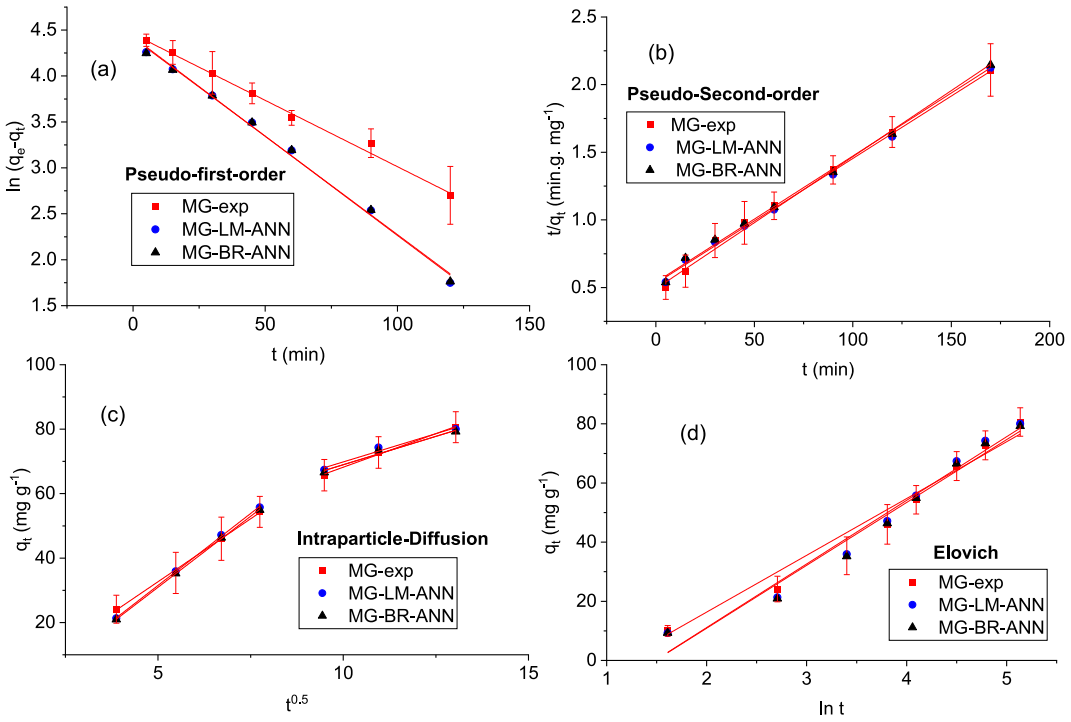

Fig. 9. (a) Pseudo-first order, (b) Pseudo-second order, (c) Intraparticle diffusion, and (d) Elovich kinetics plot fit for the adsorption of MG on CMC-SA-β-CD/NCO using experimental, and ANN predicted data.

3.7. Kinetics

The data of time and adsorption capacity was fitted into four models to obtain best suited model to describe the kinetic parameters of the adsorption of MG over CMC-SA-β-CD/NCO. The linear form of the pseudo-second-order model, pseudo-first-order model, Elovich model, and Intraparticle diffusion model is given in Eq. (12), Eq. (13), Eq. (14), and Eq. (15), respectively [55–58].

$$\underset{\text{model}}{\frac{t}{q_t} = \frac{1}{K_2\, q_e^2} + \frac{t}{q_e}\ \text{Pseudo-second-order}} \tag{12}$$

$$\underset{\text{model}}{\log(q_e - q_t) = \log q_e - \frac{k_1 t}{2.303}\ \text{Pseudo-first-order}} \tag{13}$$

$$\underset{\text{model}}{q_t = \frac{ln\, a_e b_e}{b_e} + \frac{1}{b_e} ln\, t\ \text{Elovich}} \tag{14}$$

$$\underset{\text{model}}{q_t = k_p t^{0.5} + C\ \text{Intraparticle diffusion}} \tag{15}$$

Where t = time; q_t = adsorption capacity at 't' time; k_1 = pseudo-first order constant; k_2 = pseudo-first order constant; k_p = intraparticle diffusion constant; a_e;b_e = Elovich constants; C = related to the thickness of boundary layer. Slope and interceptions of various plots yield different parameters for the adsorption of MG onto CMC-SA-β-CD/NCO.

The Pseudo-second-order model assumes a uniform coverage with chemisorption adsorption and the adsorption rate is almost insignificant compared to the initial adsorption rate [59]. Elovich model is a good fit for surfaces with heterogeneity and chemisorption and it assumes an exponential decrease in the rate of adsorption with increased adsorbate dose [60–64] Although it helps explain adsorption on very heterogeneous adsorbents, the Elovich equation does not predict any specific adsorption mechanism [60, 63,64]. The intraparticle diffusion assumes intraparticle diffusion to be rate controlling step in a single straight line that passes through the origin [65].

All four studied kinetic models were suitable for describing the adsorption of MG using CMC-SA-β-CD/NCO adsorbent (Fig. 9). The various parameters obtained using these methods are reported in Table 5. The best kinetic model was selected based on the linear correlation coefficient and closer value of $q_{e,\,cal}$ to $q_{e,\,exp}$ [22]. Although both pseudo-first order and pseudo-second order kinetics had

Table 5
Kinetics parameters for the adsorption of MG onto CMC-SA-β-CD/NCO using experimental and ANN predicted data.

Kinetic model	Parameter	MG	LM	BR
Pseudo-first order	k_1 (min^{-1})	(3.30 ± 0.12)E−2	(4.97 ± 0.14)E−2	(4.93 ± 0.14)E−2
	$q_{e,cal}$ (mg g^{-1})	86.7 ± 2.9	83.5 ± 3.3	82.6 ± 3.3
	R^2	0.993	0.996	0.996
Pseudo-second order	k_2 (g mg^{-1} min^{-1})	(1.78 ± 0.08)E−4	(1.60 ± 0.05)E−4	(1.61 ± 0.06)E−4
	$q_{e,cal}$ (mg g^{-1})	104.9 ± 2.8	108.3 ± 2.3	107.3 ± 2.5
	R^2	0.994	0.997	0.996
Intraparticle diffusion	k_{p1} (mg g^{-1} $min^{-0.5}$)	7.97 ± 0.15	8.56 ± 0.20	8.40 ± 0.22
	C_1 (mg g^{-1})	−7.55 ± 0.82	−10.7 ± 1.1	−10.4 ± 1.2
	R^2	0.999	0.998	0.998
	k_{p2} (mg g^{-1} $min^{-0.5}$)	4.16 ± 0.28	3.50 ± 0.54	3.52 ± 0.52
	C_2 (mg g^{-1})	26.6 ± 3.02	34.8 ± 6.0	33.8 ± 5.9
	R^2	0.995	0.977	0.972
Elovich	a (mg g^{-1} min^{-1})	5.04 ± 1.18	4.88 ± 1.15	4.80 ± 1.16
	b (g mg^{-1})	(4.81 ± 0.31)E−2	(4.65 ± 0.30)E−2	(4.70 ± 0.31)E−2
	R^2	0.968	0.972	0.971

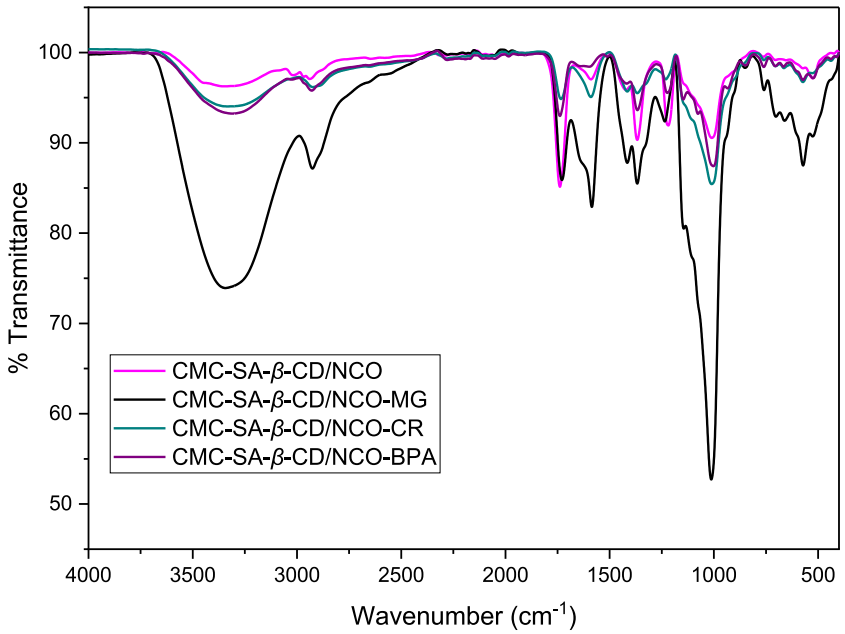

Fig. 10. FTIR spectrum of CMC-SA-β-CD/NCO before and after MG, CR, and BPA adsorption.

closer linear regression coefficients, the calculated adsorption capacity ($q_{e,\ cal}$) obtained using the pseudo-first-order kinetic model was closer to the experimental adsorption capacity ($q_{e,\ exp}$ = 81 mg g^{-1}). Hence, the adsorption of MG onto CMC-SA-β-CD/NCO follows pseudo-first-order kinetics more than pseudo-second-order kinetics. The intraparticle diffusion model does not exhibit a single linear line but two discrete linear lines (Fig. 9 (c)). This suggests that the adsorption of MG on the composite surface was controlled by more than one process. Moreover, the line does not pass through the origin, indicating that intraparticle diffusion was not the only rate-controlling step in the uptake of MG by CMC-SA-β-CD/NCO. The first initial linear line was observed for the first 60 min of contact between MG and composite and a second straight line was observed after 1 h (i.e., between 61 and 170 min). During the initial stage ~61 % MG was already adsorbed on the CMC-SA-β-CD/NCO's surface and ~29 % MG dye is adsorbed in the second stage (k_{p1}>k_{p2}). Different stages could arise due to the surface adsorption and then diffusion of MG. The best kinetic fit with pseudo-first/second kinetic order points towards chemisorption of MG onto composite surface which is in agreement with isotherm data.

3.8. Thermodynamics

The thermodynamics parameters of the adsorption process were calculated using Eq. (16) and Eq. (17).

$$\Delta G^0 = \Delta H - T\Delta S \tag{16}$$

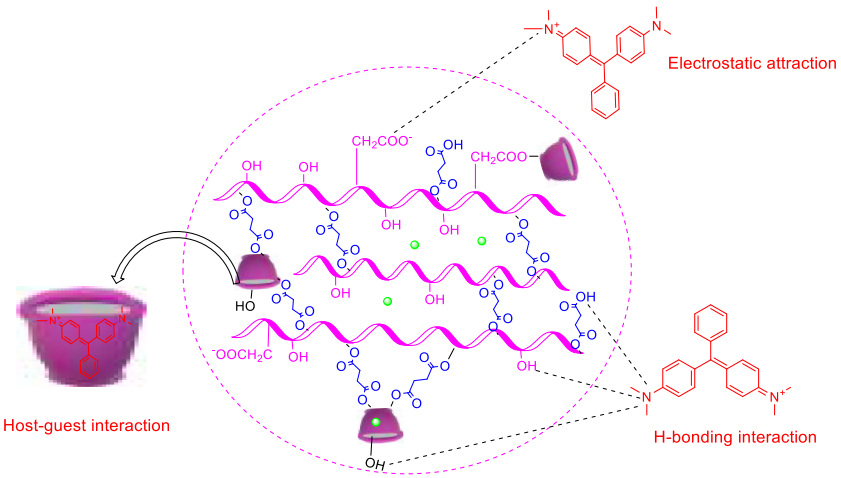

Fig. 11. Plausible interactions between MG and CMC-SA-*β*-CD/NCO nanocomposite.

$$\ln K_e = \frac{\Delta S^0}{R} - \frac{\Delta H^0}{RT} \tag{17}$$

Where ΔG° = free energy change corresponding to the MG adsorption; ΔS° = entropy change; ΔH° = enthalpy change; $Ke = q_e/C_e$.

The plot of $\ln K_e$ vs $1/T$ for calculating the thermodynamic parameters is provided in the supplementary file (Fig. S11). The plot had a linear correlation of 0.994 and 0.0163 RMSE. The adsorption of MG onto CMC-SA-*β*-CD/NCO was accompanied by heat release indicated by negative ΔH° value (-9.93 ± 0.76 kJ mol^{-1}) and ΔS° value of 0.00234 ± 0.00242 kJ mol^{-1} K^{-1}. The ΔG° was -10.6, -10.7, and -10.7 kJ mol^{-1} indicating the spontaneous adsorption of MG onto the composite surface.

3.9. FTIR of the CMC-SA-β-CD/NCO after adsorption

The FTIR spectrum of CMC-SA-*β*-CD/NCO before and after adsorption is depicted in Fig. 10. The FTIR spectrum of CR and BPA loaded CMC-SA-*β*-CD/NCO does not differ much. However, evident variation was observed in the FTIR spectrum of MG-loaded composite (CMC-SA-*β*-CD/NCO-MG), which confirmed the successful loading of MG onto CMC-SA-*β*-CD/NCO. No major shift after adsorption was observed. However, a small shift in the peak corresponding to C═O and C–H stretching was observed in all three cases. Slight shifting in peak corresponding to 1590 cm^{-1} was observed for MG and BPA. This suggests the weak interactions between MG and composite could be responsible for the adsorption. The peak at 1219 cm^{-1} in CMC-SA-*β*-CD/NCO was shifted to 1237 cm^{-1} in CMC-SA-*β*-CD/NCO-MG.

3.10. Plausible adsorption interactions

From the zeta-potential measurements, the negative surface of CMC-SA-*β*-CD/NCO was confirmed. The surface becomes negatively charged due to the deprotonation of hydroxyl and –CH_2COO^- groups within the composite. The cationic dye MG contains quaternary ammonium nitrogen. Therefore, the electrostatic interaction is possible between MG and CMC-SA-*β*-CD/NCO [46]. Moreover, *β*-CD can trap MG molecules in its cavity promoting the uptake of MG by the nanocomposite. The presence of non-bonding electron pairs on tertiary N of MG makes the H-bonding interaction with hydrogen attached to electronegative oxygen on the composite's surface possible. Therefore, major three interactions that could have contributed to the adsorption of MG onto CMC-SA-*β*-CD/NCO include electrostatic attraction, H-bonding, and host-guest interactions with the *β*-CD cavity (Fig. 11). Moreover, the presence of NCO may have facilitated weaker interaction forces between MG and nanocomposite in additional to providing weaker interaction between metal centre and N of MG.

3.11. Regeneration and reusability of CMC-SA-β-CD/NCO composite

The investigation of the reusability of the adsorbent after regeneration is crucial for determining the feasibility of its application. In the present study, the CMC-SA-*β*-CD/NCO was regenerated using acetone solvent. Acetone was able to effectively desorb the MG adsorbed on the surface of the CMC-SA-*β*-CD/NCO. The details of the same are provided somewhere else [44]. The adsorbent was studied up to five regeneration reuse cycles and the *R%* of MG was slightly declined with the number of regeneration reuse cycles (Fig. S13). As discussed in the previous section, mostly H-bonding, electrostatic attraction and host-guest interaction may have contributed to the adsorption of MG on the surface of the composite. Some MG molecules may have moved away from less firmly attached sites, while a smaller portion of MG in the MG-CMC-SA-*β*-CD/NCO compound might have stayed in the more strongly interacting sites. This could result in fewer active adsorption sites being available on the CMC-SA-*β*-CD/NCO composite, contributing

Table 6
Comparison of various adsorbents utilized in the literature for the removal of MG.

Adsorbent	q_m (mg g^{-1})	q_e (mg g^{-1})	Exo/ Endo	Advantage	Disadvantage	Ref.
CMC-SA-β-CD/ NCO	182 ± 4	86.7 ± 2.9	Exo	Ecofriendly sorbent containing high biodegradable saccharide content	Slow equilibrium and *R%* were highly affected in the presence of salt	Present work
β-CDPZF	649.4 ± 11.2	6.778 ± 1.694	Endo	Faster equilibrium and use of biodegradable β-CD	Use of less eco-friendly epichlorohydrin	[44]
CMC-g-P(AAm)	158.1	11.56	Endo	Use of environment friendly and biodegradable CMC	Slow equilibrium and low equilibrium adsorption capacity	[21]
CMC-g-P(AAm)/ MMT composite	172.4	9.878	Endo	Use of environment friendly and biodegradable CMC	Slow equilibrium and low equilibrium adsorption capacity	[21]
PVA/CMC/SA/ ZSM-5	29.58	6.100	Exo	Use of all ecofriendly materials	Low adsorption, slow equilibrium, and equilibrium capacity	[22]
Natural red clay	84.75	18–46	Endo	Use of natural material, good BET surface area, and fast equilibrium	No mention of the use of clay after the number of regeneration reuse cycles	[68]
Biochar	208.33	53.022	Endo	Use of waste sheep manure and good Langmuir adsorption capacity	High adsorption energy and lack of regeneration studies of the adsorbent	[69]
Mesoporous carbon	2000	2500	Not given	Very high BET surface area, Langmuir, and equilibrium adsorption capacity	Regeneration and reusability data were not provided, the synthesis can be slightly costly for removal applications, use of less eco-friendly materials	[66]
iso-M modified with MWCNTs and Pd	6.337–21.16	49.73	Endo	Faster equilibrium, high BET surface area, not much decline in *R%* of MG after 3–5 cycles	Low Langmuir and equilibrium adsorption capacity, the adsorbent is less environment friendly	[67]
iso-M modified using MWCNTs	3.15–18.84	49.81	Endo			
iso-M	3.274–11.05	50.16	Endo			
Imidazole based hydrogels	714.28	833.33	Not given	Good adsorption efficiency, selectivity, and reusability	Slow adsorption equilibrium and use of all synthetic materials create biodegradability issues after their usage	[70]
Graphene	196–342	13.59–166.67	Exo	Preparation of adsorbent having high BET surface area from electronic waste and hence, the overall cost of the adsorbent can be reduced	Regeneration and reusability not investigated	[71]
Slag	1787–1891	200–540.1	Endo	High uptake of MG and use of waste material as an adsorbent	No reusability investigation and presence of high metal content in the slag-waste adsorbent	[72]
Slag treated with HCl	667.9	414.6	Not given			
Fe-BTC MOFs	187.24	177.31	Not given	Faster equilibrium	Optimum MG uptake conditions, stability under various adsorption conditions, and reusability of MOFs were not provided.	[73]
FMCSN	530	55.218–495.050	Not given	Use of waste-fruit peel to synthesize FMCSNand high and fast MG removal performance	Reutilization studies for MG removal not provided	[46]
UiO-66 MOF	133.33	17.04	Not given	High BET surface area with good chemical stability	Low removal performance for MG removal	[74]

to a reduction in the adsorption efficiency after multiple regeneration and reuse cycles. Moreover, from isotherm investigation, it was found that the MG forms a monolayer on the CMC-SA-β-CD/NCO composite surface, which was also in accordance with the proposed reasons for *R%* decline as well as adsorption energy >8 kJ mol^{-1}.

3.12. Comparison with other studies

Many researchers have investigated the uptake of MG using different types of adsorbent materials. Materials with high BET surface area like mesoporous activated carbon (3438 m^2/g) [66], synthesized from carbon-nanotubes show a very high physical adsorption for MG (adsorption energy <8 kJ mol^{-1}) removal as depicted in Table 6. However, the adsorbent must be reutilized after its' initial applications in order to assess its overall utilization in the adsorption application [62]. Isoreticular MOFs (iso-M) and their modifications with multiwall CNTs and Pd are reported in Table 6, the material exhibits a faster adsorption uptake for MG but the synthetic material is not so ecofriendly and suffers from low adsorption capacity. Moreover, MOFs often suffer from stability related issues [67]. The disadvantages and advantages of these adsorbents compared to CMC-SA-β-CD/NCO are reported in Table 6.

4. Conclusion

In this study, Nickel cobaltite was synthesized using bottle gourd peel waste extract. A biopolymer-based polymeric material incorporating β-CD and CMC crosslinked with succinic acid was successfully created. The NCO was incorporated into the polymeric matrix leading to the formation of the composite CMC-SA-β-CD/NCO. Notably, this composite displayed a low BET surface area and a substantial cavity on its surface. Moreover, the composite exhibited superior thermal stability compared to the polymeric material. The adsorption behavior of MG by CMC-SA-β-CD/NCO followed pseudo-second-order kinetics, achieving an equilibrium adsorption capacity of 80–87 mg g^{-1}, with a removal efficiency exceeding 90 %. Although intraparticle diffusion played a role, it was not the sole rate-limiting step. The composite demonstrated the ability to adsorb a maximum of 178–186 mg per 1 g CMC-SA-β-CD/NCO, forming a monolayer on the heterogeneous composite surface, a characteristic often observed in chemisorption. The adsorption energy calculations also pointed towards the chemisorption of MG onto the nanocomposite surface. ANN results closely aligned with experimental data, suggesting its potential use for predicting MG uptake by CMC-SA-β-CD/NCO. The dominant interaction driving higher adsorption of MG onto the nanocomposite surface was electrostatic. However, the equilibrium was not rapid, and the presence of salt significantly reduced the removal efficiency of CMC-SA-β-CD/NCO. Despite these challenges, the composite's eco-friendly, safe, cost-effective, and biocompatible nature provides an advantage over traditional adsorbents like activated carbons.

Data availability statement

Data is provided in the manuscript and the supplementary file.

CRediT authorship contribution statement

Ruksana Sirach: Writing – original draft, Methodology, Investigation, Formal analysis, Data curation. **Pragnesh N. Dave:** Writing – review & editing, Resources, Project administration.

Declaration of competing interest

The authors declare that they have no known competing financial interests or personal relationships that could have appeared to influence the work reported in this paper.

Acknowledgments

The authors are grateful to UGC-CPEPA and UGC, New Delhi for UGC-CAS- phase-II (F-540/5/CAS-II/2018 (SAP-I)) for providing chemical facilities and UGC-CPEPA for TGA facility. The authors acknowledge the research and instrumentation facilities provided by the Department of Chemistry, Sardar Patel University. The XRD, SEM, and FTIR investigations were conducted at the Material Research Centre, Malaviya National Institute of Technology, Jaipur. Surface Area And Porosity Measurement (BET) was carried out at CSMCRI, Bhavnagar. The authors thank IICISST, Vallabh Vidyanagar for DLS measurement.RS is grateful to NMDFC and MOMA, India, for MANF-JRF (No. F. 82-27/2019 (SA-III) dated July 31, 2020).

Appendix A. Supplementary data

Supplementary data to this article can be found online at https://doi.org/10.1016/j.heliyon.2024.e33820.

References

[1] R. Foroutan, S.J. Peighambardoust, D.C. Boffito, B. Ramavandi, Sono-photocatalytic activity of cloisite 30B/ZnO/Ag2O nanocomposite for the simultaneous degradation of crystal violet and methylene blue dyes in aqueous media, Nanomaterials 12 (2022) 3103, https://doi.org/10.3390/nano12183103.
[2] P. Mohammadzadeh Pakdel, S.J. Peighambardoust, N. Arsalani, H. Aghdasinia, Safranin-O cationic dye removal from wastewater using carboxymethyl cellulose-grafted-poly(acrylic acid-co-itaconic acid) nanocomposite hydrogel, Environ. Res. 212 (2022) 113201, https://doi.org/10.1016/j.envres.2022.113201.
[3] S.J. Peighambardoust, D.C. Boffito, R. Foroutan, B. Ramavandi, Sono-photocatalytic activity of sea sediment@400/ZnO catalyst to remove cationic dyes from wastewater, J. Mol. Liq. 367 (2022) 120478, https://doi.org/10.1016/j.molliq.2022.120478.
[4] M.A. Uddin, M.S. Begum, M. Ashraf, A.K. Azad, A.C. Adhikary, M.S. Hossain, Water and chemical consumption in the textile processing industry of Bangladesh, PLOS Sustain. Transform. 2 (2023) e0000072, https://doi.org/10.1371/journal.pstr.0000072.
[5] R. Gopinathan, J. Kanhere, J. Banerjee, Effect of malachite green toxicity on non target soil organisms, Chemosphere 120 (2015) 637–644, https://doi.org/10.1016/j.chemosphere.2014.09.043.
[6] T. Li, D. Tian, Z. Zhu, W. Jin, S. Wu, H. Li, The gut microbiota: a new perspective on the toxicity of malachite green (MG), Appl. Microbiol. Biotechnol. 103 (2019) 9723–9737, https://doi.org/10.1007/s00253-019-10214-5.
[7] J. Kanhere, R. Gopinathan, J. Banerjee, Cytotoxicity and genotoxicity of malachite green on non-target aquatic organisms: chlorella pyrenoidosa and Daphnia magna, Water. Air. Soil Pollut. 225 (2014) 2134, https://doi.org/10.1007/s11270-014-2134-3.
[8] R. Sinha, R. Jindal, Elucidation of malachite green induced behavioural, biochemical, and histo-architectural defects in *Cyprinus carpio,* as piscine model, Environ. Sustain. Indic. 8 (2020) 100055, https://doi.org/10.1016/j.indic.2020.100055.

[9] S.A. Majeed, K.S.N. Nambi, G. Taju, S. Vimal, C. Venkatesan, A.S.S. Hameed, Cytotoxicity, genotoxicity and oxidative stress of malachite green on the kidney and gill cell lines of freshwater air breathing fish Channa striata, Environ. Sci. Pollut. Res. 21 (2014) 13539–13550, https://doi.org/10.1007/s11356-014-3279-8.

[10] R. Foroutan, S.J. Peighambardoust, S. Ghojavand, S. Farjadfard, B. Ramavandi, Cadmium elimination from wastewater using potato peel biochar modified by ZIF-8 and magnetic nanoparticle, Colloid Interface Sci. Commun. 55 (2023) 100723, https://doi.org/10.1016/j.colcom.2023.100723.

[11] R. Foroutan, S.J. Peighambardoust, S. Ghojavand, M. Foroughi, A. Ahmadi, F. Bahador, B. Ramavandi, Development of a magnetic orange seed/Fe3O4 composite for the removal of methylene blue and crystal violet from aqueous media, Biomass Convers. Biorefinery (2023), https://doi.org/10.1007/s13399-023-04692-x.

[12] R. Sirach, P. Dave, in: S. Thomas, A. AR, C. Jose Chirayil, B. Thomas (Eds.), Biopolymer-Based Nanocomposites for the Treatment of Organic Pollutants from the Synthetic Wastewater, Handb. Biopolym., Springer Nature, Singapore, 2023, pp. 655–684, https://doi.org/10.1007/978-981-19-0710-4_24.

[13] M.S. Rahman, M.S. Hasan, A.S. Nitai, S. Nam, A.K. Karmakar, M.S. Ahsan, M.J.A. Shiddiky, M.B. Ahmed, Recent developments of carboxymethyl cellulose, Polymers 13 (2021) 1345, https://doi.org/10.3390/polym13081345.

[14] A.S. Eltaweil, G.S. Elgarhy, G.M. El-Subruiti, A.M. Omer, Carboxymethyl cellulose/carboxylated graphene oxide composite microbeads for efficient adsorption of cationic methylene blue dye, Int. J. Biol. Macromol. 154 (2020) 307–318, https://doi.org/10.1016/j.ijbiomac.2020.03.122.

[15] X. Wang, X. Fan, H. Xie, X. Li, C. Hao, Polyacrylic acid/carboxymethyl cellulose/activated carbon composite hydrogel for removal of heavy metal ion and cationic dye, Cellulose 29 (2022) 483–501, https://doi.org/10.1007/s10570-021-04286-8.

[16] D. Allouss, Y. Essamlali, O. Amadine, A. Chakir, M. Zahouily, Response surface methodology for optimization of methylene blue adsorption onto carboxymethyl cellulose-based hydrogel beads: adsorption kinetics, isotherm, thermodynamics and reusability studies, RSC Adv. 9 (2019) 37858–37869, https://doi.org/10.1039/C9RA06450H.

[17] W. Zhu, X. Jiang, K. Jiang, F. Liu, F. You, C. Yao, Fabrication of reusable carboxymethyl cellulose/graphene oxide composite aerogel with large surface area for adsorption of methylene blue, Nanomaterials 11 (2021) 1609, https://doi.org/10.3390/nano11061609.

[18] H. Mittal, A. Al Alili, P.P. Morajkar, S.M. Alhassan, GO crosslinked hydrogel nanocomposites of chitosan/carboxymethyl cellulose – a versatile adsorbent for the treatment of dyes contaminated wastewater, Int. J. Biol. Macromol. 167 (2021) 1248–1261, https://doi.org/10.1016/j.ijbiomac.2020.11.079.

[19] C. Liu, A.M. Omer, X. Ouyang, Adsorptive removal of cationic methylene blue dye using carboxymethyl cellulose/k-carrageenan/activated montmorillonite composite beads: isotherm and kinetic studies, Int. J. Biol. Macromol. 106 (2018) 823–833, https://doi.org/10.1016/j.ijbiomac.2017.08.084.

[20] M. Rethinasabapathy, S.-M. Kang, I. Lee, G.-W. Lee, S.K. Hwang, C. Roh, Y.S. Huh, Layer-structured POSS-modified Fe-Aminoclay/Carboxymethyl cellulose composite as a superior adsorbent for the removal of radioactive cesium and cationic dyes, Ind. Eng. Chem. Res. 57 (2018) 13731–13741, https://doi.org/10.1021/acs.iecr.8b02764.

[21] S.J. Peighambardoust, O. Aghamohammadi-Bavil, R. Foroutan, N. Arsalani, Removal of malachite green using carboxymethyl cellulose-g-polyacrylamide/montmorillonite nanocomposite hydrogel, Int. J. Biol. Macromol. 159 (2020) 1122–1131, https://doi.org/10.1016/j.ijbiomac.2020.05.093.

[22] S. Radoor, J. Karayil, A. Jayakumar, J. Parameswaranpillai, S. Siengchin, An efficient removal of malachite green dye from aqueous environment using ZSM-5 zeolite/polyvinyl alcohol/carboxymethyl cellulose/sodium alginate bio composite, J. Polym. Environ. 29 (2021) 2126–2139, https://doi.org/10.1007/s10924-020-02024-y.

[23] Y. Fei, H. Deng, G. Wu, M. Luo, Y. Chen, X. Wang, H. Ye, T. Liu, Insight into adsorption process and mechanisms of Cr(III) using carboxymethyl cellulose-g-poly (acrylic acid-co-acrylamide)/attapulgite composite hydrogel, Environ. Technol. 0 (2022) 1–15, https://doi.org/10.1080/09593330.2022.2082325.

[24] N. Singh, S. Yadav, S.K. Mehta, A. Dan, In situ incorporation of magnetic nanoparticles within the carboxymethyl cellulose hydrogels enables dye removal, J. Macromol. Sci. Part A 59 (2022) 271–284, https://doi.org/10.1080/10601325.2022.2026788.

[25] Y. Zhou, T. Li, J. Shen, Y. Meng, S. Tong, Q. Guan, X. Xia, Core-Shell structured magnetic carboxymethyl cellulose-based hydrogel nanosorbents for effective adsorption of methylene blue from aqueous solution, Polymers 13 (2021) 3054, https://doi.org/10.3390/polym13183054.

[26] M. Zirak, A. Abdollahiyan, B. Eftekhari-Sis, M. Saraei, Carboxymethyl cellulose coated Fe3O4@SiO2 core–shell magnetic nanoparticles for methylene blue removal: equilibrium, kinetic, and thermodynamic studies, Cellulose 25 (2018) 503–515, https://doi.org/10.1007/s10570-017-1590-5.

[27] M. Heidari Nia, S. Ashkar, J.G. Munguia-Lopez, J. Kinsella, T.G.M. van de Ven, Hairy nanocellulose-based supramolecular architectures for sustained drug release, Biomacromolecules 24 (2023) 2100–2117, https://doi.org/10.1021/acs.biomac.2c01514.

[28] K. Kaur, R. Jindal, A comparative study of the interactions of 5-fluorouracil and Amlodipine Besylate in aqueous β-cyclodextrin solution and drug release studies, Polym. Bull. (2023), https://doi.org/10.1007/s00289-023-04859-6.

[29] K.M. Sahu, S. Patra, S.K. Swain, Host-guest drug delivery by β-cyclodextrin assisted polysaccharide vehicles: a review, Int. J. Biol. Macromol. 240 (2023) 124338, https://doi.org/10.1016/j.ijbiomac.2023.124338.

[30] V.S. Ghorpade, A.V. Yadav, R.J. Dias, Citric acid crosslinked β-cyclodextrin/carboxymethylcellulose hydrogel films for controlled delivery of poorly soluble drugs, Carbohydr. Polym. 164 (2017) 339–348, https://doi.org/10.1016/j.carbpol.2017.02.005.

[31] K.A. Uyanga, O.P. Okpozo, O.S. Onyekwere, W.A. Daoud, Citric acid crosslinked natural bi-polymer-based composite hydrogels: effect of polymer ratio and beta-cyclodextrin on hydrogel microstructure, React. Funct. Polym. 154 (2020) 104682, https://doi.org/10.1016/j.reactfunctpolym.2020.104682.

[32] M.A. Rafiq, A. Javed, M.N. Rasul, M. Nadeem, F. Iqbal, A. Hussain, Structural, electronic, magnetic and optical properties of AB2O4 (A = Ge, Co and B = Ga, Co) spinel oxides, Mater. Chem. Phys. 257 (2021) 123794, https://doi.org/10.1016/j.matchemphys.2020.123794.

[33] V.E. Bello, O.A. Olafadehan, Comparative investigation of RSM and ANN for multi-response modeling and optimization studies of derived chitosan from Archachatina marginata shell, Alex. Eng. J. 60 (2021) 3869–3899, https://doi.org/10.1016/j.aej.2021.02.047.

[34] F.N. Azad, M. Ghaedi, A. Asfaram, A. Jamshidi, G. Hassani, A. Goudarzi, M.H.A. Azqhandi, A. Ghaedi, Optimization of the process parameters for the adsorption of ternary dyes by Ni doped FeO(OH)-NWs–AC using response surface methodology and an artificial neural network, RSC Adv. 6 (2016) 19768–19779, https://doi.org/10.1039/C5RA26036A.

[35] H. Mazaheri, M. Ghaedi, M.H.A. Azqhandi, A. Asfaram, Application of machine/statistical learning, artificial intelligence and statistical experimental design for the modeling and optimization of methylene blue and Cd(II) removal from a binary aqueous solution by natural walnut carbon, Phys. Chem. Chem. Phys. 19 (2017) 11299–11317, https://doi.org/10.1039/C6CP08437K.

[36] A.F. Belhaj, K.A. Elraies, M.S. Alnarabiji, F.A. Abdul Kareem, J.A. Shuhli, S.M. Mahmood, H. Belhaj, Experimental investigation, binary modelling and artificial neural network prediction of surfactant adsorption for enhanced oil recovery application, Chem. Eng. J. 406 (2021) 127081, https://doi.org/10.1016/j.cej.2020.127081.

[37] P.S. Pauletto, S.F. Lütke, G.L. Dotto, N.P.G. Salau, Forecasting the multicomponent adsorption of nimesulide and paracetamol through artificial neural network, Chem. Eng. J. 412 (2021) 127527, https://doi.org/10.1016/j.cej.2020.127527.

[38] Y. Bao, M. Qin, Y. Yu, L. Zhang, H. Wu, Facile fabrication of porous NiCo2O4 nanosheets with high adsorption performance toward Congo red, J. Phys. Chem. Solids 124 (2019) 289–295, https://doi.org/10.1016/j.jpcs.2018.10.001.

[39] Y. Tian, H. Li, Z. Ruan, G. Cui, S. Yan, Synthesis of NiCo2O4 nanostructures with different morphologies for the removal of methyl orange, Appl. Surf. Sci. 393 (2017) 434–440, https://doi.org/10.1016/j.apsusc.2016.10.053.

[40] J. Bhagwan, G. Nagaraju, B. Ramulu, S.C. Sekhar, J.S. Yu, Rapid synthesis of hexagonal NiCo2O4 nanostructures for high-performance asymmetric supercapacitors, Electrochim. Acta 299 (2019) 509–517.

[41] H. Wang, Z. Li, S. Yahyaoui, H. Hanafy, M.K. Seliem, A. Bonilla-Petriciolet, G. Luiz Dotto, L. Sellaoui, Q. Li, Effective adsorption of dyes on an activated carbon prepared from carboxymethyl cellulose: experiments, characterization and advanced modelling, Chem. Eng. J. 417 (2021) 128116, https://doi.org/10.1016/j.cej.2020.128116.

[42] J.F. Pereira, B.M. Marim, S. Mali, Chemical modification of cellulose using a green route by reactive extrusion with citric and succinic acids, Polysaccharides 3 (2022) 292–305, https://doi.org/10.3390/polysaccharides3010017.

[43] G.A. Gebresas, T. Szabó, K. Marossy, Effects of acidity, number of hydroxyl group, and carbon chain length of carboxylic acids on starch cross-linking, Curr. Res. Green Sustain. Chem. 6 (2023) 100354, https://doi.org/10.1016/j.crgsc.2022.100354.

[44] R. Sirach, P.N. Dave, β -Cyclodextrin polymer/zinc ferrite nanocomposite: synthesis, characterization, and adsorption application for the removal of malachite green and Congo red, J. Hazard. Mater. Adv. 10 (2023) 100300, https://doi.org/10.1016/j.hazadv.2023.100300.
[45] V.V. Kutarov, E. Robens, YuI. Tarasevich, E.V. Aksenenko, Adsorption hysteresis at low relative pressures, Theor. Exp. Chem. 47 (2011) 163–168, https://doi.org/10.1007/s11237-011-9198-6.
[46] F. Tang, H. Yu, S. Yassin Hussain Abdalkarim, J. Sun, X. Fan, Y. Li, Y. Zhou, K. Chiu Tam, Green acid-free hydrolysis of wasted pomelo peel to produce carboxylated cellulose nanofibers with super absorption/flocculation ability for environmental remediation materials, Chem. Eng. J. 395 (2020) 125070, https://doi.org/10.1016/j.cej.2020.125070.
[47] S.B. Bothara, S. Singh, Thermal studies on natural polysaccharide, Asian Pac. J. Trop. Biomed. 2 (2012) S1031–S1035, https://doi.org/10.1016/S2221-1691(12)60356-6.
[48] G. Priya, U. Narendrakumar, I. Manjubala, Thermal behavior of carboxymethyl cellulose in the presence of polycarboxylic acid crosslinkers, J. Therm. Anal. Calorim. 138 (2019) 89–95, https://doi.org/10.1007/s10973-019-08171-2.
[49] R.k. Abbas, M.A. AL-Da'amy, Study of removal Malachite Green dye from aqueous solution using snail shell powder as low-cost adsorbent, IOP Conf. Ser. Mater. Sci. Eng. 928 (2020) 052011, https://doi.org/10.1088/1757-899X/928/5/052011.
[50] I. Savva, O. Marinica, C.A. Papatryfonos, L. Vekas, T. Krasia-Christoforou, Evaluation of electrospun polymer–Fe3O4 nanocomposite mats in malachite green adsorption, RSC Adv. 5 (2015) 16484–16496, https://doi.org/10.1039/C4RA16938G.
[51] X. Guo, J. Wang, Comparison of linearization methods for modeling the Langmuir adsorption isotherm, J. Mol. Liq. 296 (2019) 111850, https://doi.org/10.1016/j.molliq.2019.111850.
[52] Y.C. Wong, Y.S. Szeto, W.H. Cheung, G. McKay, Pseudo-first-order kinetic studies of the sorption of acid dyes onto chitosan, J. Appl. Polym. Sci. 92 (2004) 1633–1645, https://doi.org/10.1002/app.13714.
[53] K.H. Chu, Revisiting the Temkin isotherm: dimensional inconsistency and approximate forms, Ind. Eng. Chem. Res. 60 (2021) 13140–13147, https://doi.org/10.1021/acs.iecr.1c01788.
[54] F. Carrasco-Marin, M.V. Lopez-Ramon, C. Moreno-Castilla, Applicability of the Dubinin-Radushkevich equation to carbon dioxide adsorption on activated carbons, Langmuir 9 (1993) 2758–2760, https://doi.org/10.1021/la00035a002.
[55] S.H. Chien, W.R. Clayton, Application of Elovich equation to the kinetics of phosphate release and sorption in soils, Soil Sci. Soc. Am. J. 44 (2) (1980) 265–268, https://doi.org/10.2136/sssaj1980.03615995004400020013x.
[56] Y.S. Ho, G. McKay, Pseudo-second order model for sorption processes, Process Biochem. 34 (5) (1999) 451–465, https://doi.org/10.1016/S0032-9592(98)00112-5.
[57] Y.S. Ho, G. Mckay, Kinetic models for the sorption of dye from aqueous solution by wood, Process Saf Environ Prot 76 (2) (1998) 183–191, https://doi.org/10.1205/095758298529326.
[58] W.J. Weber, J.C. Morris, Kinetics of adsorption on carbon from solution, J. Sanit. Eng. Div. 89 (2) (1963) 31–59, https://doi.org/10.1061/JSEDAI.0000430.
[59] Y.S. Ho, G. McKay, The kinetics of sorption of divalent metal ions onto sphagnum moss peat, Water Res. 34 (2000) 735–742, https://doi.org/10.1016/S0043-1354(99)00232-8.
[60] K.U. Ahamad, R. Singh, I. Baruah, H. Choudhury, M.R. Sharma, Equilibrium and kinetics modeling of fluoride adsorption onto activated alumina, alum and brick powder, Groundw. Sustain. Dev. 7 (2018) 452–458, https://doi.org/10.1016/j.gsd.2018.06.005.
[61] G.W. Kajjumba, S. Emik, A. Öngen, H.K. Ö, S. Aydın, G.W. Kajjumba, S. Emik, A. Öngen, H.K. Ö, S. Aydın, Modelling of Adsorption Kinetic Processes—Errors, Theory and Application, IntechOpen, 2018, https://doi.org/10.5772/intechopen.80495.
[62] A.N. Ebelegi, N. Ayawei, D. Wankasi, Interpretation of adsorption thermodynamics and kinetics, Open J. Phys. Chem. 10 (2020) 166–182, https://doi.org/10.4236/ojpc.2020.103010.
[63] E. Bulut, M. Özacar, İ.A. Şengil, Equilibrium and kinetic data and process design for adsorption of Congo Red onto bentonite, J. Hazard Mater. 154 (2008) 613–622, https://doi.org/10.1016/j.jhazmat.2007.10.071.
[64] H. Qiu, L. Lv, B. Pan, Q. Zhang, W. Zhang, Q. Zhang, Critical review in adsorption kinetic models, J. Zhejiang Univ. - Sci. 10 (2009) 716–724, https://doi.org/10.1631/jzus.A0820524.
[65] W.H. Cheung, Y.S. Szeto, G. McKay, Intraparticle diffusion processes during acid dye adsorption onto chitosan, Bioresour. Technol. 98 (2007) 2897–2904, https://doi.org/10.1016/j.biortech.2006.09.045.
[66] I. Ali, I. Burakova, E. Galunin, A. Burakov, E. Mkrtchyan, A. Melezhik, D. Kurnosov, A. Tkachev, V. Grachev, High-speed and high-capacity removal of methyl orange and malachite green in water using newly developed mesoporous carbon: kinetic and isotherm studies, ACS Omega 4 (2019) 19293–19306, https://doi.org/10.1021/acsomega.9b02669.
[67] F. Borousan, F. Yousefi, M. Ghaedi, Removal of malachite green dye using IRMOF-3–MWCNT-OH–Pd-NPs as a novel adsorbent: kinetic, isotherm, and thermodynamic studies, J. Chem. Eng. Data 64 (2019) 4801–4814, https://doi.org/10.1021/acs.jced.9b00298.
[68] F. Sevim, O. Lacin, E.F. Ediz, F. Demir, Adsorption capacity, isotherm, kinetic, and thermodynamic studies on adsorption behavior of malachite green onto natural red clay, Environ. Prog. Sustain. Energy 40 (2021) e13471, https://doi.org/10.1002/ep.13471.
[69] M.F. Dilekoğlu, Malachite green adsorption from aqueous solutions onto biochar derived from sheep manure: adsorption kinetics, isotherm, thermodynamic, and mechanism, Int. J. Phytoremediation 24 (2022) 436–446, https://doi.org/10.1080/15226514.2021.1951656.
[70] E.D. Aracier, O. Aydın Urucu, E. Çakmakçi, Imidazole modified acrylate-containing photocured hydrogels for the efficient removal of malachite green dye from aqueous solutions, J. Appl. Polym. Sci. 138 (2021) 51415, https://doi.org/10.1002/app.51415.
[71] B. Karunanithi, S.K. Kannaiyan, K. Balakrishnan, S. Muralidharan, G. Gopi, Adsorption of brilliant blue and malachite green by nano-graphene exfoliated from waste batteries, Chem. Eng. Technol. 44 (2021) 1877–1889, https://doi.org/10.1002/ceat.202100213.
[72] Y. Dong, F. Guo, R. Shu, K. Dong, Q. Qiao, S. Liu, L. Xu, Y. Bai, Evaluation of the high metals-containing coal gasification fine slag as a high-performance adsorbent for malachite green adsorption, Waste Biomass Valorization 13 (2022) 4897–4909, https://doi.org/10.1007/s12649-022-01831-9.
[73] G.R. Delpiano, D. Tocco, L. Medda, E. Magner, A. Salis, Adsorption of malachite green and alizarin red S dyes using Fe-btc metal organic framework as adsorbent, Int. J. Mol. Sci. 22 (2021) 788, https://doi.org/10.3390/ijms22020788.
[74] F. Ahmadijokani, R. Mohammadkhani, S. Ahmadipouya, A. Shokrgozar, M. Rezakazemi, H. Molavi, T.M. Aminabhavi, M. Arjmand, Superior chemical stability of UiO-66 metal-organic frameworks (MOFs) for selective dye adsorption, Chem. Eng. J. 399 (2020) 125346, https://doi.org/10.1016/j.cej.2020.125346.